

Joint calibration of multi-scale hydrological data sets using probabilistic water balance data fusion: methodology and application to the irrigated Hindon River Basin, India

Roya Mourad¹, Gerrit Schoups¹, Vinnarasi Rajendran², Wim Bastiaanssen^{1,3}

5

¹Faculty of Civil Engineering and Geosciences, Delft University of Technology, Mekelweg 5, Delft, 2628 CD, the Netherlands

²Civil Engineering Department, Indian Institute of Technology Roorkee, Roorkee, Uttarakhand-, India

³Hydrosat, Wageningen, Agro Business Park 10, 6708 PW, the Netherlands.

Correspondence to: Roya Mourad (r.mourad@tudelft.nl)

10 **Abstract.** Hydrological data sets have vast potential for water resource management applications; however, they are subject to uncertainties. In this paper, we develop and apply a monthly probabilistic water balance data fusion approach for automatic bias correction and noise filtering of multi-scale hydrological data. The approach first calibrates the independent data sets by linking them through the water balance, resulting in hydrologically consistent estimates of precipitation (P), evaporation (E), storage (S), irrigation canal water imports (C), and river discharge (Q) that jointly close the basin-scale water balance. Next, 15 the basin-scale results are downscaled to the pixel-scale, to generate calibrated ensembles of gridded Precipitation (P) and Evaporation (E) that reflect the basin-wide water balance closure constraints. An application to the irrigated Hindon River basin in India illustrates that the approach generates physically reasonable estimates of all basin-scale variables, with average standard errors decreasing in the following order: 21 mm month⁻¹ for storage, 10 mm month⁻¹ for evaporation, 7 mm month⁻¹ for precipitation, 10 mm month⁻¹ for evaporation, 4 mm month⁻¹ for irrigation canal water imports, and 2 mm month⁻¹ for river discharge. Results show that updating the original independent data with water balance constraint information reduces 20 uncertainties by inducing cross-correlations between them. In addition, the introduced approach yields (i) hydrologically consistent gridded P and E estimates that fuse information from prior (original) data across different land use elements and (ii) statistically consistent random errors that reflect the model's confidence about P and E estimates at each grid cell. Future opportunities exist to further constrain the generated water balance variables and their associated errors within process-based 25 models and with additional data.

1 Introduction

Under a changing climate and anthropogenic activities (Wada et al., 2010), it becomes urgent to accurately estimate the water balance components. Although distant from the Earth's surface, remote sensing (RS) satellites can uniquely provide information that translates into such estimates. For example, microwave and infrared techniques are used to estimate 30 precipitation (Sun et al., 2018), evaporation can be computed using optical and thermal imagery (Zhang et al., 2016a), while changes in total water storage are obtained from the Gravity Recovery and Climate Experiment (GRACE) satellites (Wahr et

al., 2004; Rodell et al., 2009). These advancements have emerged as powerful decision-support tools, pushing hydrology in new directions by providing valuable information on the spatial distribution of water availability, use, and consumption (Hessels et al., 2022; Sheffield et al., 2018; Karimi et al., 2013). Such information is often challenging to obtain through 35 traditional in situ data collection. With the rapid increase in RS data availability, it is now theoretically possible to close the water balance. However, two challenges prevent this from being achieved, including the inconsistencies among various RS products for the same variable and the imbalances resulting from integrating the unique combinations of different water balance variables. These incoherences arise from the inherent data errors. Discrepancies in RS data, for example, come from different sources, such as errors in the retrieval algorithms (Maggioni et al., 2022), input data and parameters (Crosetto et al., 2001), or 40 scale mismatch (Foken, 2008). While in situ data are known for their greatest reliability, they also come with their own errors. Uncertainties in river discharge, for example, could be related to flow conditions (McMillan et al., 2012), velocity sensors (e.g., calibration) (Horner et al., 2018), or estimation methods such as the rating curve (Kuczera, 1996). Benefiting from the complementary strengths of in situ and RS data and embracing their errors requires a three-pronged methodology. This methodology should maximize the prior information content of the data available from multiple RS sources for the same 45 variable, quantify both systematic and random errors in each water balance term, and reduce these errors by exploiting all available information to generate calibrated estimates of spatially distributed water balance data. The following paragraphs review existing approaches in the literature used to handle these aspects.

Studies addressing the uncertainties in RS water balance data often rely on in situ data (treated as “ground-truth”) to evaluate and converge on the different data products. However, in situ data (e.g., evaporation) is sparsely measured, and even when 50 these data exist, accessibility may be challenging. Under such conditions, alternative indirect approaches such as triple collocation (Tian and Peters-Lidard, 2010; Long et al., 2014; Massari et al., 2017; Yin and Park, 2021), uncertainty propagation (Hong et al., 2006; Cawse-Nicholson et al., 2020), and sensitivity analyses (Sobol, 2001) can be utilized. Other methods involve using the deviation from the ensemble mean, and the variability between the data sets as a proxy for uncertainty (Tian and Peters-Lidard, 2010; Sahoo et al., 2011; Munier et al., 2014; Zhang et al., 2018). Each of the previously summarized error 55 estimation techniques has its inherent merits and shortcomings. In an attempt to capitalize on these strengths, Mourad et al. (2024) recently integrated limited in situ data and multiple error metrics, along with expert judgment, to quantify and partially reduce water balance data errors. However, the resulting water balance estimates require further conditioning on in situ data using additional constraining steps, which is a subject of the methodology section of the current study.

Several other studies went beyond quantifying uncertainties in RS data and sought to fully reduce them using the water balance 60 as a constraint (Aires, 2014; Hobeichi et al., 2020; Luo et al., 2023; Munier et al., 2014; Pan et al., 2012; Pan and Wood, 2006; Rodell et al., 2015; Sahoo et al., 2011; Zhang et al., 2018; Zhang et al., 2016b). The core idea of the existing closure methods is to either select a preferred single data set of each water balance variable based on prior knowledge about their quality, or merge multiple data for each water balance variable using fixed pre-quantified error estimates. This step is followed by a water balance correction method such as variational data assimilation (L'ecuyer and Stephens, 2002), constrained Kalman filter (Pan 65 and Wood, 2006), or proportional redistribution (Abolafia-Rosenzweig et al., 2021). In this process, the values of the

(un)merged water balance estimates are adjusted proportionally to their relative uncertainties or magnitudes, depending on the correction method used. Contrary to the previously summarized water balance closure approaches, which fixed data errors a priori, Schoups and Nasseri (2021) proposed improving data error estimation by treating them along with the water balance variables as unknown random variables. Instead of enforcing the closure sequentially, the authors demonstrate that the water
70 balance variables can be calibrated simultaneously in a single probabilistic data fusion methodology. The underlying premise is that all variables are interconnected through the water balance. For instance, to calibrate precipitation data, the proposed approach uses statistical inference techniques to automatically fuse and adjust two information sources available on this variable, one coming from multiple estimates of precipitation RS data (original prior data), and the other sourced from other water balance data (predicted from the water balance). These techniques include an iterative smoother that involves multiple
75 forward-backward passes over the timeseries. In the forward pass, the estimated precipitation carries information from previous and current months, while in the backward pass it holds information from the future months. A similar process happens when estimating the other water balance variables, yielding refined posterior estimates that combine information from all other months.

Further to the above literature, previous attempts have been made to extend the basin-wide water balance closure constraints
80 to a finer scale of up to 0.25° pixel resolution (Barkhordari et al., 2025; Heberger et al., 2023; Pellet et al., 2019; Munier et al., 2014). Building on these previous efforts, our emphasis here is on generating detailed calibrated precipitation (0.05° resolution) and evaporation (250 meters resolution) estimates that align with the basin-scale closure constraints. To that end, we intend to contribute to the literature by extending the existing basin-scale water balance data fusion method first introduced by Schoups and Nasseri (2021). The extended methodology presented here retains the original model's key advantages, namely: the ability
85 to simultaneously calibrate the basin-wide water balance variables by exploiting data from the entire timeseries. An integral part of this new version is using the basin-wide posteriors to generate calibrated ensembles of spatially distributed precipitation and evaporation. This is achieved in a stepwise procedure, with the first step involving the formulation of ensemble-driven grid-scale error models, contrary to the models in Schoups and Nasseri (2021), which were formulated at the basin-scale and relied on an ensemble of two data sets. The second step is a constraint step carried out by the water balance data fusion at the
90 basin scale, yielding basin-scale posteriors for all water balance variables, and a Kalman smoothing algorithm, yielding grid-scale posteriors for precipitation and evaporation. This approach ensures consistency across the two scales: when back-calculating the basin-scale estimates from the grid-scale posteriors via spatial averaging, we recover the inferred basin-scale posteriors from the water balance data fusion. Lastly, the new version of the methodology incorporates the following additional features: (i) accounting for surface water imports from irrigation canals, which might significantly affect the overall water
95 budget in irrigated basins, and (ii) quantifying posterior cross-correlations between water balance variables, which is important for generating joint posterior samples. We apply the extended approach to an irrigated monsoon-influenced Hindon Basin, which suffers from unsustainable water use.

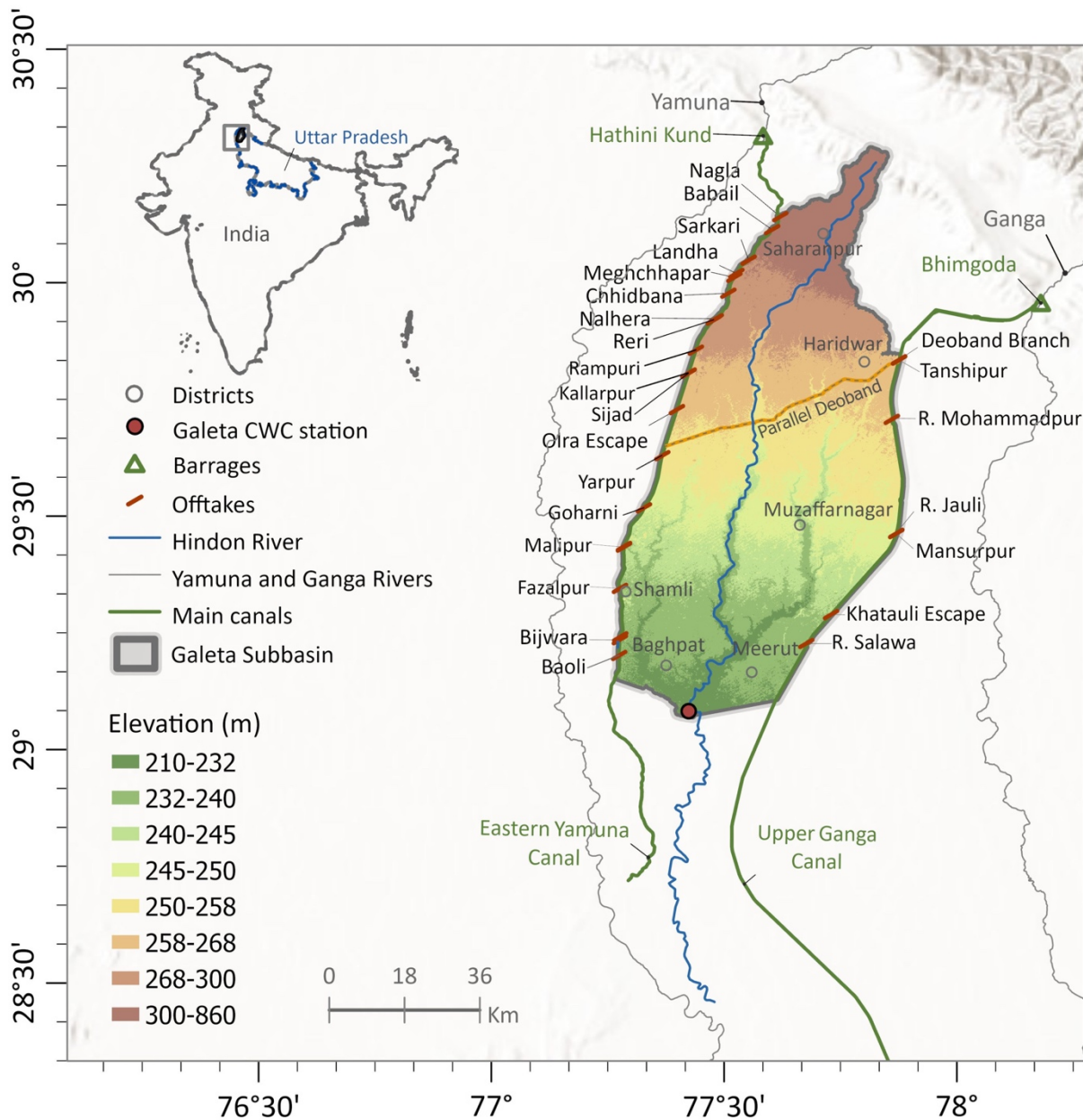
The remainder of this paper is structured as follows: section 2 introduces the case study and describes the data sets used as input for the probabilistic water balance model presented in Sect. 3. Section 4 details how all unknowns in the water balance

100 model are solved at the basin scale, yielding a closed water balance, and how these water balance constraints are transferred to the grid scale. The basin and grid-scale results are then presented in Sect. 5. The sensitivity of the water balance data fusion approach to the modeling decisions is then discussed in Sect. 6. Throughout the paper, we use the terms “priors” and “posteriors” to refer to the variables (i.e., water balance terms and error parameters) before and after calibration, respectively (i.e., before and after introducing the monthly water balance constraints).

105 **2 Case Study: Hindon Basin in Northern India**

The study focuses on the Hindon Basin in the northwestern Uttar Pradesh State of India (see Fig. 1). The Hindon basin covers a total area of about 4780 km² and drains to the Galeta outlet, where a river discharge station is located. The rainfed Hindon River originates from the Shivalik Hills at the foothills of the Himalayas. It flows towards the south on the flat and alluvial surfaces of the basin. The river eventually drains into the Yamuna River (near Noida, downstream of Delhi), which, in turn, 110 joins the Ganga River before it reaches the Bay of Bengal. The basin features a large-scale supply-based irrigation system with two major irrigation canals: the Eastern Yamuna Canal (EYC) and the Upper Ganga Canal (UGC). These canals are fed by two external reservoirs located outside the basin, namely the Bhimgoda Barrage constructed on the Ganga River and Hathni Kund Headwork on the Yamuna River. The share of the external canal water imports in the water balance is significant for this heavily irrigated basin, representing about 30-40% of the annual precipitation (Fig. A1). In addition to supplying surface 115 irrigation water to the study area, the canals contribute to groundwater recharge through seepage, forming several groundwater mounds near their vicinity. Hence, the canals approximately coincide with groundwater divides, limiting lateral groundwater flow across the eastern and western boundaries of the Hindon basin (Umar et al., 2008).

The canal system is operated in two irrigation seasons: the Kharif and Rabi seasons. Kharif season extends from March to September, in which the main irrigated crops are sugarcane and rice, and the Rabi season spans from October to March of the 120 following year, where the principal crops are wheat and mustard. The irrigated croplands represent more than 85% of the basin, while only about 10% of the basin’s area is covered by non-croplands (Fig. A2). Irrigation water is diverted from the canals to supply the basin through off-takes [that serve fixed command areas with crops rotated between Rabi and Kharif crops](#) (Fig. 1).



125 **3 Probabilistic water balance model**
 Our goal is to estimate each term in the monthly water balance, written as:

$$S_t = S_{t-1} + \bar{P}_t - \bar{E}_t - Q_t + C_t \quad (1)$$

130 Equation (1) combines the different water balance terms together, where S_{t-1} and S_t are the total water storage in the basin at the start and end of month t (including surface storage, soil moisture, and groundwater), \bar{P}_t and \bar{E}_t are the basin-average precipitation and evaporation (including transpiration), Q_t is the river discharge at the basin outlet for month t , and C_t is the total canal water import into the basin (sum of all intakes, see Fig. 1) for month t . The net lateral groundwater flows into or out of this basin are assumed to be negligible due to their small magnitude relative to the other water balance variables (Alam and Umar, 2013). All terms in Eq. (1) are expressed in units of mm of equivalent water depth. The following paragraphs describe the water balance data for the case study.

135 Each water balance component in Eq. (1) is independently derived, gathered, or measured either from satellite data, ground-based measurements, or both (Table 1). In the prior selection of the most reliable precipitation and evaporation ensembles (see: Mourad et al. (2024)), we followed other water balance closure studies that emphasize the use of earth observations over model 140 outputs to minimize the effect of their related assumptions, except for the Multi-source Weighted-Ensemble Precipitation (MSWEP v2.8) product (Beck et al., 2019). MSWEP is an “optimal merging” of gauge observations, satellite observations, and reanalysis model output. Along with MSWEP, we use two other monthly gridded precipitation ensemble members: the Tropical Rainfall Measuring Mission (TRMM) (Huffman et al., 2007) and the NASA/JAXA Global Precipitation Measurement (GPM-IMERG) (Huffman et al., 2019). By combining precipitation radar, passive microwave, and infrared satellites with 145 ground-based observations from the Global Precipitation Climatology Centre (GPCC), TRMM and GPM-IMERG provide a comprehensive precipitation estimate over a given area. Compared to single-band radar on TRMM, GPM dual-frequency precipitation radar provides a broader range of measurable precipitation rates and a better estimate of precipitation particle size (Hou et al., 2014). Spatially interpolated rain-gauge for the basin from Indian Meteorological Department (IMD) data set (Pai et al., 2014) is included in this analysis for comparison but not used in the model.

150 For gridded evaporation ensembles, we incorporate five members with diverse methodological approaches for estimating evaporation from remote sensing. One ET data set based on two-parallel Penman-Monteith (PM) models for both canopy and soil: the pyWaPOR-ET v2.6 (Bastiaanssen et al., 2012), two ET data sets that estimate ET from a single-source surface energy balance (SEB) model representing vegetation and soil in a combined energy balance, namely the Landsat Collection 2 Provisional Actual Evapotranspiration Science Product (Landsat-based SSEBop ET) (Senay, 2018; Senay et al., 2023) and the 155 Surface Energy Balance Algorithm for Land (eeSEBAL product) (Bastiaanssen et al., 1993), in addition to a two-source SEB ALEXI-ET data set from the Atmosphere-Land Exchange Inverse model (Anderson et al., 2007; Anderson et al., 2015). We also incorporate the CMRSET ET product based on the CSIRO MODIS Reflectance-based Scaling ET model (Guerschman et al., 2009) that uses vegetation indices and meteorological data for scaling the ET. All data sets are resampled to the same spatial resolution using bilinear interpolation. More details on the theoretical background and processing steps for the P and E 160 data sets can be found in the companion paper (Mourad et al., 2024).

The total water storage variable data were obtained from the recent release of the monthly Jet Propulsion Laboratory (JPL-RL06) mascon solution. Each monthly total water storage estimate represents the surface mass anomaly relative to the baseline

average over 2004-2009. This version relies on prior geophysical information to constrain the solution, eliminating the need for empirical de-striping filtering commonly used for post-processing traditional spherical harmonic gravity solutions.

165 However, intrinsic to this product are biases, that is, leakage errors, and spatial smoothing that damps the “true” signal, especially in small-sized basins. A Coastline Resolution Improvement (CRI) filter has been applied in this version to reduce signal leakage errors across coastlines (Wiese et al., 2016). This data is also accompanied by scaling factors for optionally restoring the damped signal. However, these were not applied to the data used herein; instead, bias along with noise variance are modeled using all water balance data incorporated in this study (see Sect. 3.3). [Another storage input data set is also](#)

170 [included: GRACE Spherical Harmonic \(CSR\) solution \(Sect. 6.1\)](#) (Swenson and Wahr, 2006; Landerer and Swenson, 2012).

The in situ data used in this analysis are obtained from governmental agencies, including the Central Water Commission (CWC) of India for streamflow data and the irrigation department of Uttar Pradesh for external canal water imports data. While river discharge data has no gaps, canal delivery data are constrained by their spatial and temporal coverage. The latter comes in two forms: irrigation schedules and actual flow measurements. We apply an extrapolation approach that combines both data sources to generate complete monthly estimates for all intakes (for more details on the adopted gap-filling technique, refer to Appendix A2).

175 [As can be seen in Table 1, the native resolution of the individual data sets and between the water balance variables varies widely, posing a challenge in their merging process. In principle, the probabilistic water balance data model can be performed at any spatial resolution; however, for this study design, we try to preserve the native information as much as possible by choosing to resample all precipitation data sets to a common resolution of 0.05° and all evaporation data sets to a common resolution of 250m. An alternative design would be to resample all water balance variables to the same resolution \(e.g., 250m\), but this might introduce artefacts, for example, when up-sampling from coarse to high resolution.](#)

180 **Table 1: Monthly Water Balance Data. The data type column distinguishes between Remote Sensing (RS) and ground-based Measurements (GBM).**

Variable	Data Type	Data Source	Original (Resampled) resolution	Study period
Precipitation (P_{obs}^{obs})	RS and GBM	TRMM TMBA (TRMM3B43 v7)	0.25° (0.05°)	2003-2019
	RS and GBM	GPM (IMERG) 3IMERGDF (v06)	0.1° (0.05°)	2003-2022
	Merged	MSWEP v2.8	0.1° (0.05°)	2003-2022
Evaporation (E_{obs}^{obs})	RS	pyWaPOR v2.6	250m (250m)	2003-2022
	RS	Landsat C2 Provisional ET (Landsat-SSEBop)	30m (250m)	2003-2022
	RS	eeSEBAL	30m (250m)	2003-2022
	RS	CMRSET	5km (250m)	2003-2012
	RS	ALEXI	5km (250m)	2003-2015
Storage (S_{obs})	RS	GRACE JPL mascon (RL06 v1.0)	3° (basin-wide)	2003-2022

(S^{obs})	<u>RS</u>	<u>GRACE Spherical Harmonic (CSR)</u>	<u>1° (basin-wide)</u>	<u>2003-2022</u>
River discharge ($Q_{obs}^{obs} Q^{obs}$)	GBM	Stream gauge (Central Water Commission, 2024)	point	2003-2022
Canal Water ($C_{obs}^{obs} C^{obs}$)	GBM	Canal gauges and irrigation schedules (Irrigation & Water Resources Department, 2024)	distributary-based	2003-2022
Imports				

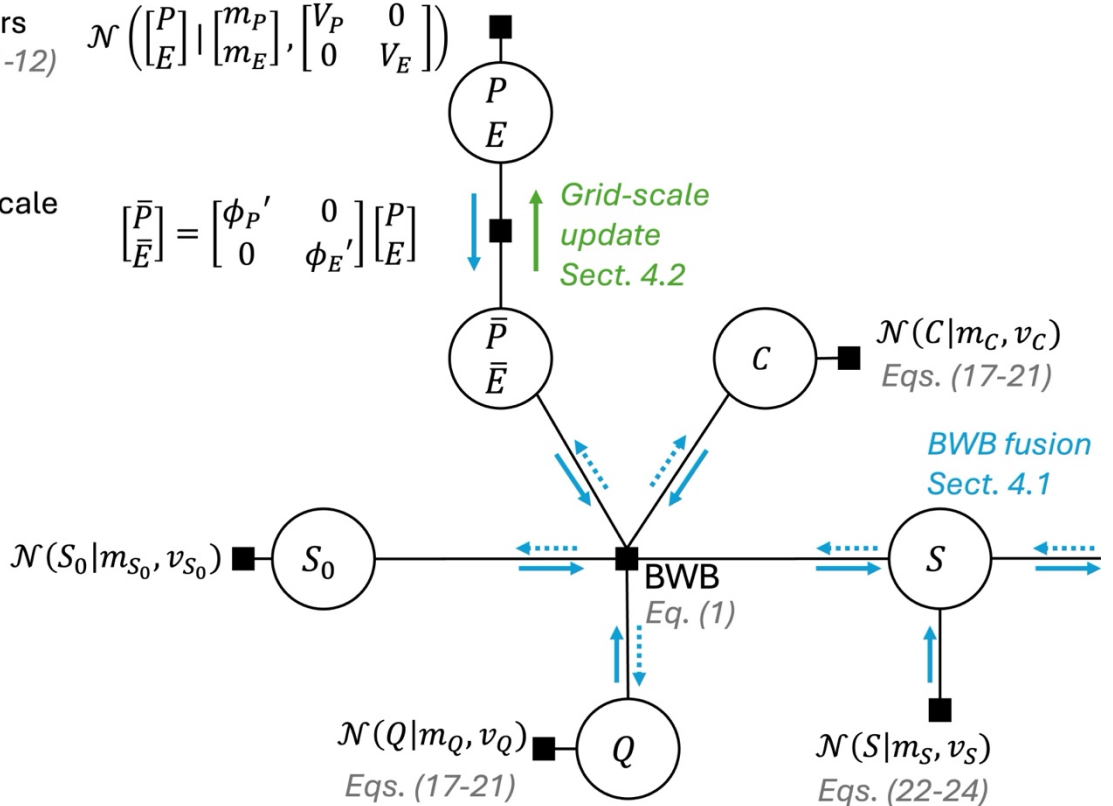
185 Despite the variety of the above-explored data sources, two barriers hinder their potential use in hydrological applications. One occurs when integrating the unique data combinations describing each water balance variable into the basin-scale water balance. In any particular month, we end up with significant errors, i.e., either too much or too little water, resulting in a non-zero net balance (Fig. B1 in Appendix B). This non-closure or imbalance problem highlights the incoherences between the water balance data sets and the inconsistencies in the individual data sets, caused by various data errors. Another well-known
190 challenge is the inconsistencies between the various data products for the same variable. For example, for the studied basin, grid-scale inter-product uncertainty is moderate for P , while E exhibits significant spatial variability across the whole basin (Mourad et al., 2024). These challenges motivate the distinction between the “calibrated” value of each water balance variable that satisfies the water balance closure at the basin scale and represents the error-corrected estimate at the grid level, and the “observed” values, which deviate from these values. In the probabilistic form of the water balance, each term is
195 assigned a probabilistic data error model to quantify systematic and random differences between observed and modelled water balance variables. Parameters in these data error models are treated as unknown random variables with predefined prior distributions. In this regard, the overall probabilistic water balance takes the form of a Bayesian hierarchical model with two levels of uncertainty: one related to the error parameters and another linked to the water balance variables (Schoups and Nasseri, 2021) (Schoups and Nasseri (2021)). Figure 2 gives an overview of the adopted methods our approach, and the
200 following The following subsections describe the parametric probabilistic relations adopted used for each water balance variable (P , E , Q , C , and S).

Grid-scale priors
Eqs. (2-6) & (11-12)

$$\mathcal{N} \left(\begin{bmatrix} P \\ E \end{bmatrix} \mid \begin{bmatrix} m_P \\ m_E \end{bmatrix}, \begin{bmatrix} V_P & 0 \\ 0 & V_E \end{bmatrix} \right)$$

Grid to basin-scale averaging
Eq. 25

$$\begin{bmatrix} \bar{P} \\ \bar{E} \end{bmatrix} = \begin{bmatrix} \phi_P' & 0 \\ 0 & \phi_E' \end{bmatrix} \begin{bmatrix} P \\ E \end{bmatrix}$$



205 **Figure 2: A factor graph showing the random variables in circles and constraints between variables as squares for a single month.**
 Three constraints are incorporated in the water balance data fusion method, including: a prior Gaussian distribution assigned to each water balance variable (squares attached to each variable), the basin-scale water balance (BWB) constraint that links all water balance variables together, and the spatial averaging constraint that links grid-scale precipitation (P) and evaporation (E) and to basin-scale variables for precipitation (\bar{P}) and evaporation (\bar{E}). Computation of posteriors of individual variables proceeds in two steps. The first step is basin-scale water balance data fusion (BWB fusion, see Sect. 4.1). This step involves multiple forward (blue arrows along the edges) and backward (dotted blue arrows) passes over the data using the entire timeseries to compute the posteriors of all water balance variables that jointly close the water balance (Schoups and Nasseri, 2021). The second step computes grid-scale posteriors for precipitation and evaporation from their basin-scale posteriors using a Kalman smoothing algorithm (green arrow, see Sect. 4.2).

3.1 Precipitation and Evaporation error models

215 Contrary to Schoups and Nasseri (2021), we define prior error models for P and E at the grid scale instead of at the basin scale. As described below, followed by spatial averaging is used to derive corresponding priors at the basin scale. The latter are then used with water balance data fusion for estimating basin-scale posteriors (Sect. 4.1). The resulting basin-scale posteriors are finally transferred back to the grid scale (Sect. 4.2).

The first step in setting up a prior error model for the gridded P and E variables is to probabilistically characterize them with

220 prior distributions. For these two independent spatial processes, we can write their grid-scale joint prior distribution for each
month t as:

$$\mathcal{N} \left(\begin{bmatrix} P_t \\ E_t \end{bmatrix} \mid \begin{bmatrix} m_{P_t} \\ m_{E_t} \end{bmatrix}, \begin{bmatrix} V_{P_t} & 0 \\ 0 & V_{E_t} \end{bmatrix} \right) \quad (2)$$

where P_t and E_t are vectors containing unknown precipitation and evaporation values for all grid cells in the corresponding
spatial field for each month t . The Gaussian distribution (Eq. (2)) is specified with a mean vector and a block diagonal
covariance matrix with zero cross-covariance to reflect that these two processes are assumed to be independent a priori. The

225 mean vector consists of the prior means of P (m_{P_t}) and E (m_{E_t}), for all spatial locations ~~s~~within the corresponding spatial
domain of each month t , while the autocovariance of each variable P (V_{P_t}) and E (V_{E_t}) is the block-diagonal element of the
covariance matrix. The decomposed form of the joint distribution for each individual variable is described in the following
subsections.

3.1.1 Precipitation

230 The independence structure between P_t and E_t shown in Eq. (2) allows us to represent the errors in each variable separately.

For each month t ~~and at each grid cell location s~~, we typically have multiple ~~measurements of~~gridded precipitation products,
with unknown bias and random errors. We use the spread across different precipitation products to define a grid-scale
precipitation error model for the prior means m_{P_t} (mean vector in Eq. 2) and the prior standard deviations s_{P_t} (vector of the
square root of all diagonal entries of the autocovariance matrix V_{P_t} in Eq. 2) To characterize these errors, the grid-scale
precipitation bias and random error models for each ~~all~~ elements in the mean vector m_{P_t} and the square root of all diagonal
entries of the autocovariance matrix V_{P_t} are defined using Eqs. (3-4), respectively:

$$m_{P_t} = (1 - w_p)P_t^{obs,min} + w_pP_t^{obs,max} \quad m_{P_{s,t}} = P_{s,t}^{obs,min} + w_p(P_{s,t}^{obs,max} - P_{s,t}^{obs,min}) \quad (3)$$

$$s_{P_t} = r_p \frac{1}{4} (P_t^{obs,max} - P_t^{obs,min}) \quad s_{P_{s,t}} = r_p \frac{1}{4} (P_{s,t}^{obs,max} - P_{s,t}^{obs,min}) \quad (4)$$

Equation (3) models the systematic bias in the gridded-scale precipitation ~~at each location s~~ for each month t by describing the
grid-scale precipitation prior means m_{P_t} as a weighted average of the minimum ($P_t^{obs,min}$) and maximum ($P_t^{obs,max}$)
precipitation for each grid cell. function of two parts. The first part represents the baseline precipitation estimated as the
240 minimum across all grid cells for the location ~~s~~products ($P_t^{obs,min}$), while the second consists of a weighted deviation
from this base value. Specifically, the latter denotes the full range of the grid-wise observed precipitation ($P_t^{obs,max} -$
 $P_t^{obs,min}$) with a weight parameter w_p . The weight or bias parameter w_p takes on an unknown value
between 0 and 1, and is estimated from the data (see section 4.1), with a logit normal prior distribution of parameter $\mu = 0$
and scale parameter $\sigma = 1.4$ to reflect prior uncertainty about the bias. In other words, w_p controls the relative position of the

245 $m_{p_t} m_{p_{s,t}}$ within the observed precipitation space (range). As it approaches 0, more weight is given to the minimum across all products ($P_t^{obs,min} P_{s,t}^{obs,min}$,), whereas approaching a value of 1 gives more weight to the maximum across all products ($P_t^{obs,max} P_{s,t}^{obs,max}$,).

250 Random errors in the grid-scale precipitation are modeled using Eq. (4). This model expresses the grid-scale prior standard deviations $s_{p_t} s_{p_{s,t}}$ at grid cell location s for each month t as a function of the difference between the maximum and minimum precipitation in each grid cell potential random error, defined as a quarter of the range: $\frac{1}{4} (P_t^{obs,max} - P_t^{obs,min} P_{s,t}^{obs,max} - P_{s,t}^{obs,min})$. A noise parameter (r_p), taking values a value between 0 and 1, is used to scale the standard deviations. This parameter is also estimated from the data this conservative quantity and is given a quasi uniform prior distribution between 0 and 1.

To account for the effect of spatial correlation of the random error component (Eq. (4)), we write the precipitation prior covariance matrix V_{p_t} in terms of the grid-scale standard deviations and a grid-scale auto-correlation matrix:

$$255 V_{p_t} = S_{p_t} R_p S_{p_t} \quad (5)$$

where S_{p_t} is a diagonal matrix containing the grid-scale $s_{p_t} s_{p_{s,t}}$ values for all locations of the spatial field (Eq. (4)), and R_p is the correlation matrix that captures the spatial dependence structure. $R_p \in \mathbb{R}^{n_p \times n_p}$, where $n_p \times n_p$ is the matrix dimension, and n_p equals 176, representing the total number of grid cell locations of the precipitation spatial domain. R_p is jointly estimated from all precipitation data using an isotropic parametric correlation function with the following form (Handcock and Stein, 1993):

$$260 C_M(d|l_s, v) = \frac{1}{2^{v-1} \Gamma(v)} \left(\frac{d}{l_s} \right)^v K_v \left(\frac{d}{l_s} \right) \quad (6)$$

where C_M is the Matérn correlation function for variables separated by distance d . This correlation model is flexible and widely used, with two functions: gamma function $\Gamma(\cdot)$ and the modified Bessel function $K_v(\cdot)$ (Abramowitz and Stegun, 1968). C_M also consists of two unknown nonnegative parameters, namely the spatial correlation length scale l_s and a spatial smoothness parameter v . A value of v approaching 0 indicates a rough spatial process, while the process is smoother when v approaches infinity. Since the smoothness parameter is usually small in many applications (Chen et al., 2022), while it increases

265 as the aggregation time increases (Sun et al., 2015), we choose a balanced value between a rough and smooth random field, i.e., v , fixed at 1.5. On the other hand, the correlation length scale (l_s) defines an average length scale on which grid cells are correlated with each other. In principle, l_s ranges from 0 (the case of uncorrelated grid cells) and extends to a scale larger than the spatial domain length (the case of maximally correlated pixels). With no prior information on the l_s parameter, we fix it at 50 km ($\sim 1/2$ the basin's length from North to South). The sensitivity of the results to the fixed l_s will be evaluated in section

270 6.2.

Since water balance data fusion (Schoups and Nasseri, 2021) uses basin-scale error models, we derive these from the above-described grid-scale models by spatial averaging. Specifically, the basin-scale prior mean $m_{\bar{p}_t}$ and variance $v_{\bar{p}_t}$ in month t follow from Eqs. 3, 4, and 5: $m_{\bar{p}_t}$ and variance $v_{\bar{p}_t}$ in month t are given by:

$$m_{\bar{p}_t} = \phi_p^t m_{p_t} = \bar{m}_{p_t} \quad (7)$$

$$v_{\bar{p}_t} = \phi_p^t V_p \phi = \bar{V}_{p_t} \quad (8)$$

$$m_{\bar{p}_t} = \phi'_p m_{P_t} = \phi'_p [(1 - w_p) P_t^{obs,min} + w_p P_t^{obs,max}] \quad (7)$$

$$v_{\bar{p}_t} = \phi'_p V_p \phi = \phi'_p S_{P_t} R_p S_{P_t} \phi_p = \phi'_p (r_p D_{P_t}) R_p (r_p D_{P_t}) \phi_p \quad (8)$$

$$\bar{P}_t \sim \mathcal{N}(m_{\bar{p}_t}, v_{\bar{p}_t}) \quad (9)$$

$$\bar{P}_t \geq 0 \quad (10)$$

275 where \bar{m}_{p_t} is the average of all elements in m_{p_t} , \bar{V}_{p_t} is the average of all elements in the matrix V_{p_t} and ϕ_p is the spatial averaging operator used to derive basin-scale moments mean and variance from grid-scale moments means and variances (i.e., $s n_p \times 1$ vector with each element equal to $1/n_p$, where $s n_p$ is the number of spatial locations in the precipitation spatial field). ϕ'_p is the transpose of ϕ_p . We also used $S_{P_t} = r_p D_{P_t}$, where D_p is a diagonal matrix containing the $\frac{1}{4}(P_t^{obs,max} - P_t^{obs,min} P_{s,t}^{obs,max} - P_{s,t}^{obs,min})$ values (from Eq. 4) and overbars denote spatial averaging (e.g., $\bar{P}_t^{obs,min}$ with a dropped s subindex, is the spatial average across for all grid cells values within the minimum precipitation spatial field). All overbar (basin-averaged) input quantities to Eqs. (7-8) are precomputed from the precipitation data sets, and the constant but unknown parameters w_p and r_p are estimated as part of the water balance data fusion (see Sect. 4.1).
280 Finally, the last two equations in the precipitation error model treat the basin-scale calibrated precipitation \bar{P}_t for each month t as a random draw from a truncated normal distribution. The truncation at zero ensures physical consistency (nonnegative precipitation).
285

Substituting the grid-scale models specified above, Eqs. (3-4), into the spatial averaging, Eqs. (7-8), yields the following basin-scale error model for precipitation:

$$m_{\bar{p}_t} = \bar{P}_t^{obs,min} + w_p (\bar{P}_t^{obs,max} - \bar{P}_t^{obs,min}) \quad (9)$$

$$s_{\bar{p}_t} = r_p \sqrt{D_p R_p D_p} \quad (10)$$

$$\bar{P}_t \sim \mathcal{N}(m_{\bar{p}_t}, s_{\bar{p}_t}^2) \quad (11)$$

$$\bar{P}_t \geq 0 \quad (12)$$

where D_p is a diagonal matrix containing the $\frac{1}{4}(P_{s,t}^{obs,max} - P_{s,t}^{obs,min})$ values and overbars denote spatial averaging (e.g.,

290 $\bar{P}_t^{obs,min}$ with a dropped s subindex, is the spatial average across all grid cell values within the minimum precipitation field).

All overbar (basin averaged) quantities are precomputed from the precipitation data sets, and the constant but unknown parameters w_E and r_E are estimated as part of the water balance data fusion (see Sect. 4.1).

Finally, the last two equations in the precipitation error model treat the basin-scale calibrated precipitation \bar{P}_t for each month t as a random draw from a truncated normal distribution. The truncation at zero ensures physical consistency (nonnegative precipitation).

3.1.2 Evaporation

As with precipitation, an evaporation error model with the following range-based form is adopted:

$$m_{E_t} = f_E [(1 - w_E)E_t^{obs,min} + w_E E_t^{obs,max}] m_{E_{s,t}} = f_E [E_{s,t}^{obs,min} + w_E (E_{s,t}^{obs,max} - E_{s,t}^{obs,min})] \quad (4311)$$

$$s_{E_t} = r_E \frac{1}{4} (E_t^{obs,max} - E_t^{obs,min}) s_{E_{s,t}} = r_E \frac{1}{4} (E_{s,t}^{obs,max} - E_{s,t}^{obs,min}) \quad (4412)$$

The systematic bias in grid-scale evaporation is modeled with two spatial and time-invariant calibration parameters, namely: w_E and f_E . The parameter w_E is the a bias parameter or weight that interpolates between the monthly grid-scale evaporation extrema $E_t^{obs,min}$ and $E_t^{obs,max}$ $E_{s,t}^{obs,min}$ and $E_{s,t}^{obs,max}$ at each grid cell location s and month t . w_E takes on a value between 0 and 1, and is estimated from the data (see section 4.1). An additional scaling factor (f_E) is incorporated to account for potential bias outside the observed grid-scale evaporation range, and is given a lognormal prior with mode at 1 (no bias) and a coefficient of variation CV of 50%.

On the other hand, Eq. (4412) quantifies the random errors in grid-scale evaporation, as the difference between the maximum and minimum evaporation in each grid cell. A prior uncertainty ($\frac{1}{4} (E_{s,t}^{obs,max} - E_{s,t}^{obs,min})$) scaled via the spatially and temporally constant noise parameter (r_E), taking a value between 0 and 1, is used to scale the random errors. All parameters are solved as part of the water balance data fusion (Sect. 4), treated as random variables with prior distributions. The w_E and r_E parameters are specified with a vague prior distribution bounded between 0 and 1, specifically, flat logit normal with location parameter $\mu = 0$ and scale parameter $\sigma = 1.4$. Whereas, f_E is given a lognormal prior with mode at 1 (no bias) and a coefficient of variation CV of 50%. Notably, all unknown parameters are solved as part of the water balance data fusion (Sect. 4).

The basin-scale error models are derived from the grid-based models defined above, using the same spatial averaging process applied to precipitation (Eqs. (7-8)). The averaging formulas are then obtained as follows:

$$m_{\bar{E}_t} = \phi'_E m_{E_t} = f_E \phi'_E [(1 - w_E)E_t^{obs,min} + w_E E_t^{obs,max}] f_E [E_t^{obs,min} + w_E (E_t^{obs,max} - E_t^{obs,min})] \quad (4513)$$

$$s_{\bar{E}_t} = r_E \sqrt{D_E R_E D_E} v_{\bar{E}_t} = \phi'_E V_{E_t} \phi_E = \phi'_E S_{E_t} R_E S_{E_t} \phi_E = \phi'_E (r_E D_{E_t}) R_E (r_E D_{E_t}) \phi_E \quad (4614)$$

$$\bar{E}_t \sim \mathcal{N}(m_{\bar{E}_t}, v_{\bar{E}_t}) \quad (47-15)$$

$$\bar{E}_t \geq 0 \quad (48-16)$$

where D_E is a diagonal matrix whose diagonal entries are ~~contain the $\frac{1}{4}(E_t^{obs,max} - E_t^{obs,min}) \frac{1}{4}(E_{s,t}^{obs,max} - E_{s,t}^{obs,min})$ grid-based values for all grid cells within the evaporation spatial domain. In, $\bar{E}_t^{obs,min}$, $\bar{E}_t^{obs,max}$ and $\sqrt{D_E R_E D_E}$ are the prior quantities. All inputs of Eqs. (13-14) are precomputed from the evaporation data sets, computed from the evaporation data sets through spatial averaging. ϕ_E is the spatial averaging operator, and the R_E term. The R_E term in the last quantity~~ 320 stands for the correlation matrix, which captures the spatial dependencies between the evaporation grid cells. $R_E \in \mathbb{R}^{n_E \times n_E}$, where $n_E \times n_E$ is the matrix dimension, and n_E equals 71059, representing the total number of grid cell locations of the evaporation spatial domain. For the large-sized evaporation data sets considered here, we parameterize the evaporation correlation matrix R_E , here, using a Matérn kernel implemented within a stochastic variational Gaussian Process (Hensman et al., 2015) with fixed parameter l_s at 50 km and ν at 1.5.

325 Similar to precipitation, the basin-scale calibrated evaporation \bar{E}_t for month t is treated as a random draw from a truncated normal distribution Eqs. (47-15-48-16). The truncation at zero ensures physical consistency (nonnegative evaporation).

3.2 River discharge and canal water import error models

We ~~assume that data use the same proportional error model to relate on the river discharge (Q^{obs}) and canal water imports (C^{obs}) are both unbiased with proportional random errors (Eq. (18)) observations to their modeled values. Both variables are modelled as truncated Gaussian variables (non-negative), with mean m_{x_t} , standard deviation s_{x_t} , and standard deviation variance $s^2_{x_t}$ in month t given by (x here is either river discharge or canal water import). The model takes the following general form:~~ 330

$$m_{x_t} = x_t^{obs} m_{x,t} \sim \mathcal{N}(x_{obs,t}^{obs}, v_{obs,t}^{obs}) \quad (49-17)$$

$$s_{x,t} = a_x x_t^{obs} a_x + b_x \quad (20-18)$$

$$v_{x_t} = s_{x,t}^2 \quad (19)$$

$$x_t \sim \mathcal{N}(m_{x_t}, v_{x_t} s_{x,t}^2) \quad (24-20)$$

$$x_t \geq 0 \quad (22-21)$$

where x_t^{obs} represents the observed variable of interest value for each month t (Q_t^{obs} for discharge and C_t^{obs} for canal water imports). Given the complete Q^{obs} records and gap-filled C^{obs} data, for each month, we set $v_t^{obs} v_{obs,t} = 0$, such that

335 $m_{x,t} m_{x,t}$ becomes equal to the observed (unbiased) data (x_t^{obs}) for that specific month. The standard deviation $s_{x_t} s_{x,t}$

represents quantifies the the random errors in the $Q^{obs} Q_{obs}$ and or $C^{obs} C_{obs}$, and is assumed proportional to the observed value, with proportionality constant (or relative error) a_x . These errors are modeled as a linear function defined by two time invariant parameters: a_x (slope) and b_x (intercept). This suggests that as the magnitude of the variable of interest increases, its potential random error also increases. We assume tight prior constraints on a_x and b_x to reflect the strong prior belief on these measurements. We assume a 10% relative error for monthly river discharge, i.e. $a_Q = 0.1$, and a 25% relative error for canal water imports, i.e. $a_C = 0.25$. Namely, a_x is assigned a lognormal prior with a mode at 0.1 for $Q^{obs} Q_{obs}$ and 0.25 for $C^{obs} C_{obs}$ (i.e., a relative error of 10% and 25%, respectively) and a small CV of 1%, while b_x is assigned a lognormal prior with mode at 0.001 and also a CV of 1%. Schoups and Nasseri (2021) showed that these priors provide reasonable approximations of a_x and b_x for basins where the measured variable (here: $Q^{obs} Q_{obs}$ and $C^{obs} C_{obs}$) is small in magnitude relative to the other water balance variables.

3.3 Water Storage Error Model

A key feature of The water storage error model is that it relates the storage observations from the GRACE satellite ($S_{obs,t}^{obs}$) to the corresponding calibrated modeled storage (S_t), instead of the other way around (as in the earlier defined error models). Due to the coarse resolution of GRACE data, the monthly basin-scale total water storage derived from these observations can be polluted by the water storage dynamics occurring outside the basin, that is, “leakage”. To account for the temporal and spatial mismatch between GRACE basin-scale water storage and the calibrated modeled storage caused by leakage errors, we employ the following noisy sine wave error model (Schoups and Nasseri, 2021):

$$m_{S,t} = S_t + A \sin\left(\omega\left(\frac{t}{12} - \delta\right)\right) \quad (22)$$

$$v_{S_t} = \sigma_S^2 \quad (23)$$

$$s_S = \sigma_S \quad (24)$$

$$S_{obs,t}^{obs} \sim \mathcal{N}(m_{S,t} m_{S,t}^2, v_{S_t} s_S^2) \quad (25)$$

The first equation models the systematic errors associated with GRACE observations. It captures cyclic patterns and seasonality in the data within the basin via time-invariant error parameters. These parameters describe the magnitude and the timing of the seasonal error: the amplitude A (mm) and phase δ (years), respectively.

The second equation models the magnitude of random errors as an unknown time-invariant parameter (σ_S) , which reflects errors that can arise from (a) any limitations caused by the sine wave models in capturing the calibrated water storage dynamics within the basin and (b) noise in GRACE solutions. In the above equations, ω is fixed at 2π radians per year, yielding a one-year sine wave and thus capturing the annual seasonal cycle. Other parameters are assigned vague prior distributions where A follows a lognormal prior with mode at 30 mm and a CV of 200%, σ_S a lognormal prior with mode equal to 10 mm and a

CV of 200%, and δ follows a flat logit-normal prior between 0 and 1 year with a location parameter $\mu = 0$ and scale parameter $\sigma = 1.4$.

While the above prior error model relies on a single storage data set, we assess a posteriori (Sect. 6.1) the sensitivity of the P and E posterior distributions to the use of different storage inputs, including Mascon (JPL) and Spherical Harmonic (CSR) 365 GRACE solutions, which for the basin studied here, exhibit different ~~with considerably varying magnitudes in~~ long-term trends.

4 Inference methods

The following subsections detail the two-step statistical inference framework used to solve the basin-scale probabilistic water balance model (Sect. 4.1) and then propagate the resulting basin-wide constraints to the grid level (Sect. 4.2).

370 4.1 Basin-scale

Following the description of the prior probabilistic relations (Sect. 3), the posteriors of water balance variables and error parameters are computed using a basin-scale inference technique. This technique consists of a double-loop method that combines two algorithms: a single-chain differential evolution variant of Markov Chain Monte Carlo (DE-MCMC) for computing the unknown parameters and Expectation Propagation (EP) for solving the unknown water balance variables. A

375 brief overview of these algorithms is described in ~~the~~ Appendix B, while a detailed explanation can be found in the original paper (Schoups and Nasseri, 2021). The computed posteriors provide hydrologically consistent water balance variables that jointly close the water balance. In the water balance data fusion process, the independent prior data (Sect. 3) are updated with the monthly water balance constraints. These constraints link all independent variables through the water balance, thereby inducing cross-correlation between them. For example, the term S in the water balance constraint (dropping the time index t

380 for simplicity: $S = S_0 + \bar{P} - \bar{E} - Q + C$) linearly links all other terms. To maintain the water balance closure, the terms with opposite signs must covary together, and vice versa. [Here](#)[In this paper](#), an additional post-processing step is applied to represent this interdependence structure between the water balance variables, i.e., compute their covariances. For a vector of posterior variables x (including the initial storage state S_0 or $S_{t-1}, \bar{P}, \bar{E}, Q$, and C), a joint distribution can be written for each month t as: $p(x_t) \sim \mathcal{N}(m_{x,t}^*, V_t^*)$ with a mean vector $(m_{x,t}^*)$ holding the marginal posterior means of each variable (Eq. (B2))

385 and a 5×5 covariance matrix V_t^* that encodes the relation between these variables. The diagonal element of this matrix contains each variable's marginal posterior variance, while the unknown covariances between each variable pair are the off-diagonal entries. To quantify these covariances, a message-passing algorithm that combines the water balance constraint and the probabilistic constraints in the form of marginal Gaussian distributions is applied ([See](#)[see](#) Text B2 in Appendix B).

4.2 Grid-scale

390 Having computed the joint basin-scale \bar{P} and \bar{E} posteriors (Sect. 4.1), the goal is to translate these posteriors back to the grid-scale. When spatially averaged, the generated grid-scale posteriors (P and E) should recover the basin-scale posteriors. Such a relation between the two scales can be established for each month t as follows (Eq. (2625)):

$$\begin{bmatrix} \bar{P}_t \\ \bar{E}_t \end{bmatrix} = A \begin{bmatrix} P_t \\ E_t \end{bmatrix} \quad (2625)$$

where $A = \begin{bmatrix} \phi_P' & 0 \\ 0 & \phi_E' \end{bmatrix}$ represents the spatial averaging operator mapping the grid-scale to the basin-scale P and E variables, ϕ_P' and ϕ_E' are defined earlier in Eqs. (87 and 13), while ϕ_P is a $s \times 1$ vector with each element equal to $1/s$, where s is the number of spatial locations in the evaporation spatial domain. ϕ_P' and ϕ_E' are their transpose.

395 For the above relation to hold (Eq. (2625)), we implement a Kalman smoothing algorithm. A key aspect of this algorithm is that it ties together all sources of information on P and E variables, detailed in previous sections, including: the basin and grid-scale joint priors (Sect. 3), along with basin-scale joint posteriors (Sect. 4.1), to generate their corresponding spatially distributed joint posteriors. Distinctly, the grid-scale prior moments (Eq. (2)) are updated to reflect the difference between the 400 basin-scale joint posterior and prior moments via the Kalman gain. In what follows, we start by describing the basin-scale joint prior and posterior distributions and then show how the grid-scale joint distributions are computed.

Before constraining the basin-scale spatially averaged \bar{P}_t and \bar{E}_t priors, their joint distribution for each month t can be written with zero-cross covariances to reflect the independent structure between both variables:

$$\mathcal{N} \left(\begin{bmatrix} \bar{P}_t \\ \bar{E}_t \end{bmatrix} \mid \begin{bmatrix} m_{\bar{P}_t} \\ m_{\bar{E}_t} \end{bmatrix}, \begin{bmatrix} v_{\bar{P}_t} & 0 \\ 0 & v_{\bar{E}_t} \end{bmatrix} \right) \quad (2726)$$

where $m_{\bar{P}_t}$ and $m_{\bar{E}_t}$ are prior means, $v_{\bar{P}_t}$ and $v_{\bar{E}_t}$ are prior variances of \bar{P}_t and \bar{E}_t , respectively.

405 Once the water balance constraint is imposed within the basin-scale data fusion: $\bar{P} - \bar{E} - Q + C + S_0 - S = 0$ (omitting t for simplicity), positive correlations between \bar{P} and \bar{E} posteriors emerge. This occurs because the water balance acts as a constraint on the priors (independent \bar{P} and \bar{E}) linearly linking them in their posteriors (correlated \bar{P} and \bar{E}). To maintain this linear constraint, that is, $\bar{P} - \bar{E}$ remains equal to $Q - C - S_0 + S$, an adjustment that increases \bar{P} should be balanced by an adjustment that increases \bar{E} , and vice versa. This yields a basin-scale joint posterior distribution on the posterior variables \bar{P}_t and \bar{E}_t , with induced correlations, that is, non-zero cross covariances:

$$\mathcal{N} \left(\begin{bmatrix} \bar{P}_t \\ \bar{E}_t \end{bmatrix} \mid \begin{bmatrix} m_{\bar{P}_t}^* \\ m_{\bar{E}_t}^* \end{bmatrix}, \begin{bmatrix} v_{\bar{P}_t}^* & v_{\bar{P}\bar{E}_t}^* \\ v_{\bar{P}\bar{E}_t}^* & v_{\bar{E}_t}^* \end{bmatrix} \right) \quad (2827)$$

where $m_{\bar{P}_t}^*$ and $m_{\bar{E}_t}^*$ are the marginal posterior means, $v_{\bar{P}_t}^*$ and $v_{\bar{E}_t}^*$ are the marginal posterior variances of \bar{P}_t and \bar{E}_t , respectively, and $v_{\bar{P}\bar{E}_t}^*$ is the posterior cross-covariance between \bar{P}_t and \bar{E}_t .

415 Kalman smoothing can then be used to calculate the joint posterior moments Eqs. (29~~28~~-30~~29~~) at the grid-scale from the above basin-scale prior moments Eqs. (27~~26~~-28~~27~~) and grid-scale prior moments (Eq. (2)). These posterior moments are thus rendered as a weighted combination of grid and basin-scale moments:

$$\begin{bmatrix} m_{P_t}^* \\ m_{E_t}^* \end{bmatrix} = \begin{bmatrix} m_{P_t} \\ m_{E_t} \end{bmatrix} + K \left(\begin{bmatrix} m_{\bar{P}_t}^* \\ m_{\bar{E}_t}^* \end{bmatrix} - \begin{bmatrix} m_{\bar{P}_t} \\ m_{\bar{E}_t} \end{bmatrix} \right) \quad (29\textcolor{red}{28})$$

$$\begin{bmatrix} V_{P_t}^* & V_{PE_t}^* \\ V_{PE_t}^{*'} & V_{E_t}^* \end{bmatrix} = \begin{bmatrix} V_{P_t} & 0 \\ 0 & V_{E_t} \end{bmatrix} + K \left(\begin{bmatrix} v_{\bar{P}_t}^* & v_{\bar{P}\bar{E}_t}^* \\ v_{\bar{P}\bar{E}_t}^* & v_{\bar{E}_t}^* \end{bmatrix} - \begin{bmatrix} v_{\bar{P}_t} & 0 \\ 0 & v_{\bar{E}_t} \end{bmatrix} \right) K' \quad (30\textcolor{red}{29})$$

where $m_{P_t}^*$ and $m_{E_t}^*$ are the grid-scale means, while $V_{P_t}^*$ and $V_{E_t}^*$ are autocovariances of P_t and E_t posteriors, respectively.

$V_{PE_t}^*$ and $V_{PE_t}^{*'}$ stand for the posterior cross-covariance between both variables and its transpose, respectively.

420 A noteworthy feature of the Kalman smoothing gain (K) in the above equations is that it acts as a weighting matrix propagating basin-scale information to each individual P and E grid cell. It is computed using the following equation composed of three components:

$$K = \begin{bmatrix} V_{P_t} & 0 \\ 0 & V_{E_t} \end{bmatrix} A' \begin{bmatrix} v_{\bar{P}_t} & 0 \\ 0 & v_{\bar{E}_t} \end{bmatrix}^{-1} \quad (31\textcolor{red}{30})$$

The first component depicts the block diagonal covariance matrix of the grid-scale P_t and E_t priors, the second is the transpose of the spatial averaging operator A , whereas the inverse of the diagonal matrix consisting of the basin-wide variances of \bar{P}_t and \bar{E}_t priors is the third component.

425 5 Results

Here, we present the results of the two-step inference framework described in section 4, starting with the basin-scale posteriors of all water balance variables (Sect. 5.1) and followed by the grid-scale posteriors of P and E (Sect. 5.2). These represent the baseline results that are based on specific choices of GRACE data (i.e., JPL mascon data) and spatial correlation lengths. The sensitivity of the results to these choices will be addressed in Sect. 6.

430 5.1 Basin-scale posteriors

Basin-scale posteriors for P (precipitation), E (evaporation), and C (canal water imports) are shown in Fig. 2~~3~~ and discussed first. The data shows significant prior uncertainty with a wide range of precipitation and evaporation estimates. This is especially evident in the monsoon (June to September) for precipitation and across the whole seasonal cycle for evaporation (Fig. 2~~3~~). Along with the prior observations, Fig. 2~~3~~ also depicts the basin-scale posteriors for each water balance term, while Fig. 3~~4~~ shows the corresponding error parameter posteriors. The results for Q are not included in Fig. 2~~3~~ since the posterior for Q closely follows the river discharge data, and this data is tied to a non-disclosure agreement with the CWC of India.

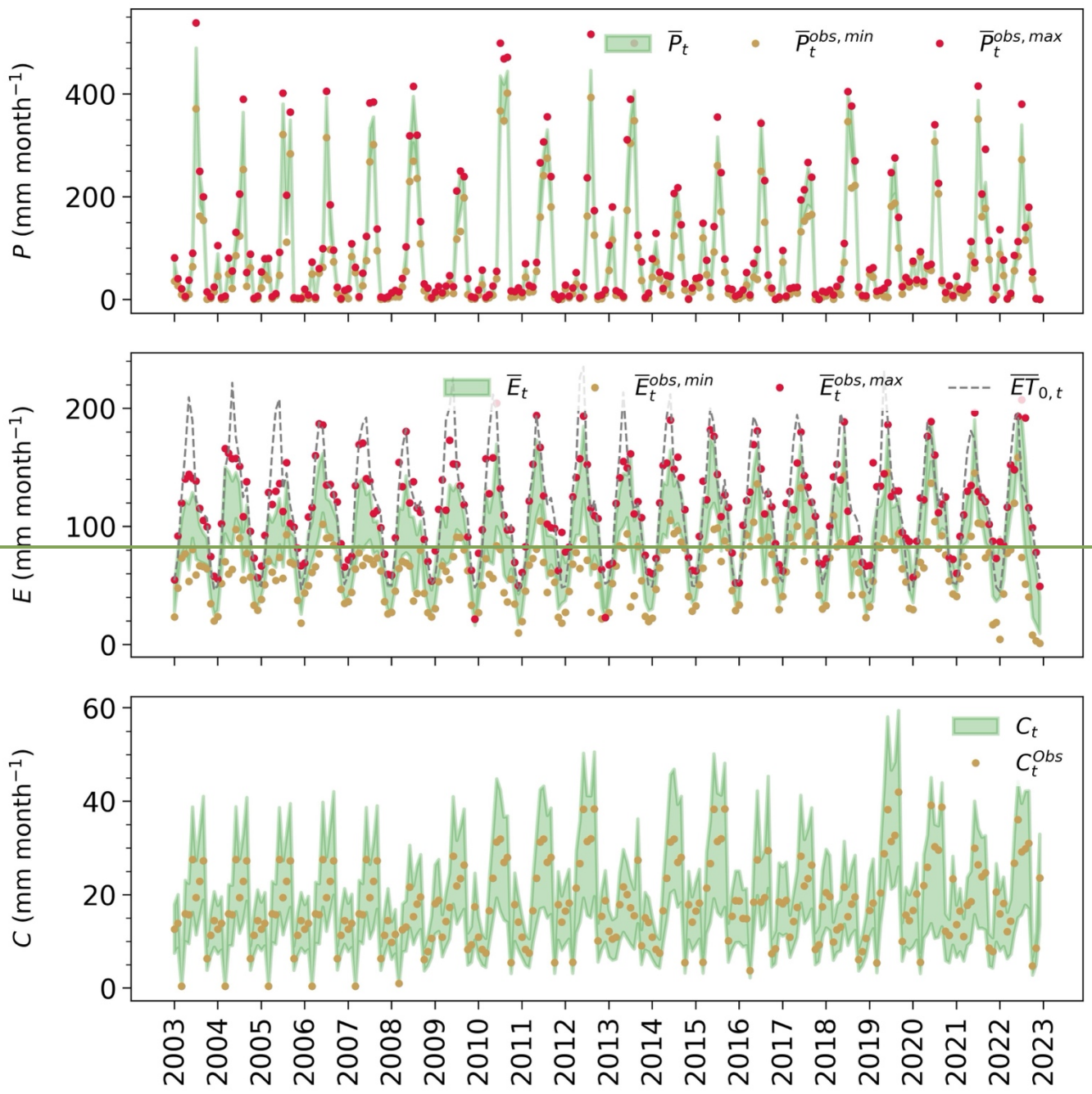
The results in Fig. 2-3 show that the precipitation posterior mean lies between the $\bar{P}_t^{obs,min}$ and $\bar{P}_t^{obs,max}$ data bounds. This balanced position within the precipitation space is also translated into the inferred parameter w_p , with a posterior distribution around values of ~ 0.5 (Fig. 3). The noise parameter r_p has a posterior distribution around 1, suggesting a minimal reduction in the prior uncertainty range for precipitation. An independent evaluation of these posterior estimates can be done by comparing them to the Indian Meteorological Department (IMD) data set (Pai et al., 2014), which is routinely used to evaluate precipitation products in India. Despite being treated as the “ground truth” in literature, the rain-gauge interpolated IMD product is not error-free, and therefore, a perfect match between the IMD data and the generated posterior mean is not anticipated. Figure C1 in Appendix C compares the seasonal and annual timeseries of the IMD to the posterior [precipitation](#) mean. Unlike the precipitation posterior mean, which tends to sit between observed data bounds, the IMD data set closely follows the baseline precipitation estimate (TRMM). The larger posterior estimates for P found here align with a recent study (Goteti and Famiglietti, 2024) that found systematic underestimation of precipitation by the IMD data product. Moving to evaporation, the computed posteriors in Fig. 2-3 only slightly differ from the priors, with posterior values of noise parameter r_E centered at ~ 0.95 (Fig. 3), implying that the modeled random error in this variable is as large as one-fourth of the absolute difference between $\bar{E}_t^{obs,min}$ and $\bar{E}_t^{obs,max}$. This posterior uncertainty, however, reduces with a tighter data range corresponding to prior ensembles generated from only three data sets: eeSEBAL, pyWaPOR, and Landsat-SSEBop (specifically, from 2015 onwards). As for the estimated evaporation, it takes more or less a balanced weight between $\bar{E}_t^{obs,min}$ and $\bar{E}_t^{obs,max}$, with an estimated w_E posterior of ~ 0.48 and a scaling parameter f_E around 1 (no additional bias). While no direct evaporation measurements are available, the posterior estimates can be evaluated by comparing them with reference evapotranspiration and expected seasonal dynamics based on known cropping and irrigation practices. For example, the evaporation is expected to be lower than \bar{ET}_0 but equal to or higher than the \bar{ET}_0 for only a short period, either in June-July or August-October, when the (dominant) sugarcane crop coefficient (K_c) exceeds 1. In Fig. 2-3, the inferred posterior evaporation (green band) aligns with this expectation where it is consistently below \bar{ET}_0 , but is also around \bar{ET}_0 for the previously mentioned period (e.g., in 2006, 2012, 2019, and 2022). Besides sugarcane, rice is the second most important crop, commonly transplanted at the end of April or mid-May (Joseph and Ghosh, 2023). For this shallow-rooted crop, more frequent irrigation is required during its early stages (the first 30 days), coinciding with the period when the canal water supplies form a peak (at the onset of the monsoon) (Fig. C3 in Appendix C). The evaporation timeseries of rice is, thus, expected to form a peak, most likely in June, when its K_c value is higher than 1. Considering these two elements, the evaporation is expected to peak in June, as captured by the posterior [evaporation](#) mean (Fig. C2 in Appendix C).

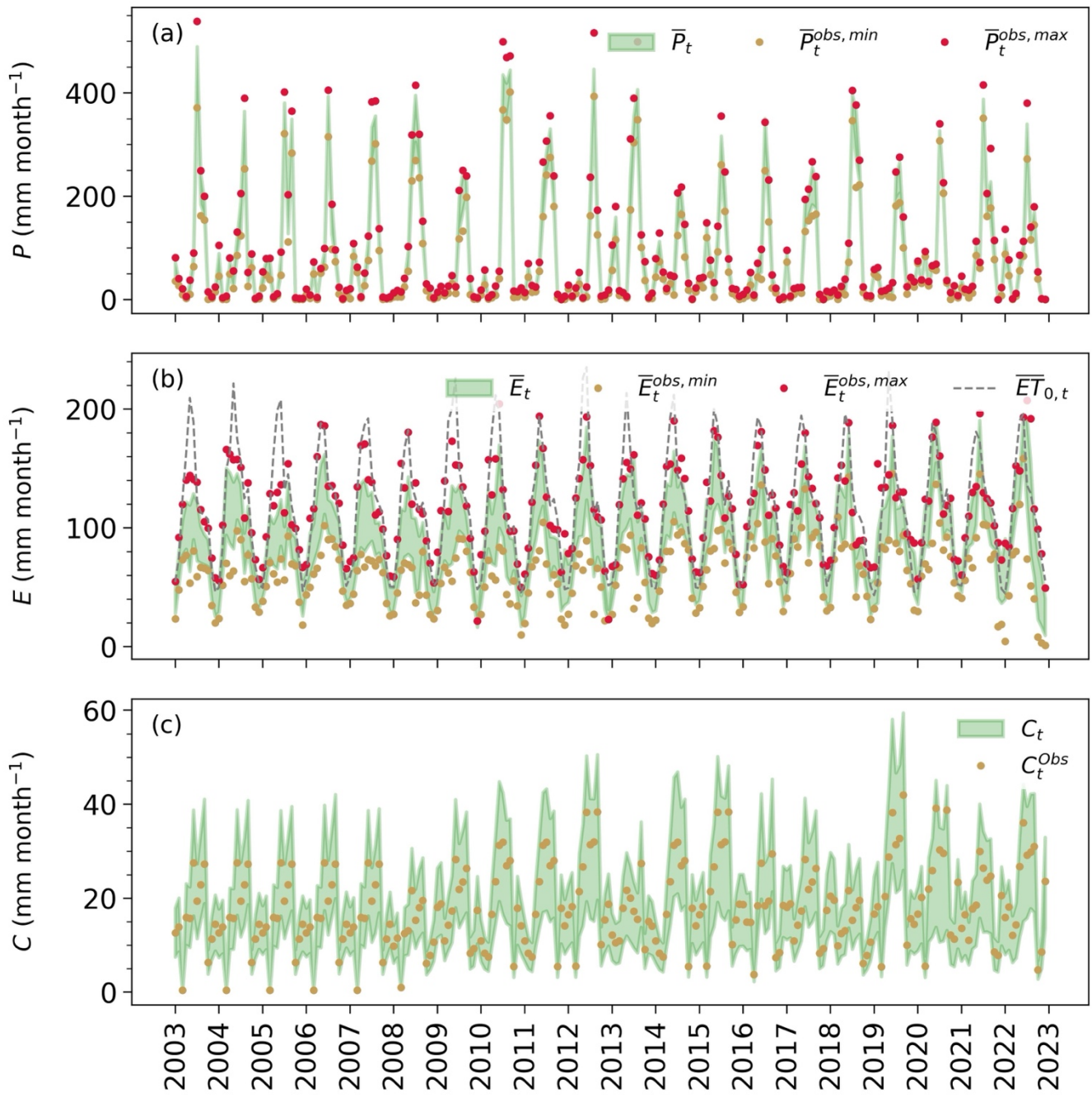
The third row of Fig. 2-3 compares the prior and posterior estimates of the canal water imports (C). The prior estimates represented here are extrapolated from scarce data. Nevertheless, the extrapolation approach mostly relied on ground-based measurements whenever available. For periods with missing data, these were filled with the design discharge capacity multiplied by the operation time [or the data average of years with similar conditions depending on data availability per distributary](#). [For this purpose, independent information from the Palmer Drought Severity Index \(PDSI\) index of the Terra](#)

470 Climate data set (Abatzoglou et al., 2018) is used as a proxy to classify the years between wet and dry. In that way, the gap-filled full timeseries of the canal water imports can be seen as upper bound estimates. The applied extrapolation approach also, allowing allows for annual variations in the canal water supply, by using independent information from the Palmer Drought Severity Index (PDSI) index of Terra Climate data set (Abatzoglou et al., 2018) as a proxy to classify the years between wet and dry. For example, in dry years, such as 2008, and 2016 to 2018, the surface water supplies are smaller in magnitude compared to all other years. Note also the increase in the water supplies from 2009 onwards, which aligns with the construction of the Deoband Parallel Canal that connects the Upper Ganga Canal (UGC) to the Eastern Yamuna Canal (EYC) (Fig. 1). Using other approaches to generate and extrapolate the prior canal water estimates does not significantly affect the posteriors of the other terms, as explored in Sect. 6.3. The posterior results, on the other hand, reflect the wide prior uncertainty (relative error of 25%) we place around this extrapolated data. Generally, the posterior estimates follow both their priors and the 480 seasonality of the precipitation term. Specifically, the supplies peak at the onset of the monsoon (June) due to increased water availability from precipitation, while smaller peaks are formed during the dry season (Dec and April) when water stored in the reservoirs is diverted for irrigation. As canal supplies are mainly driven by precipitation, it is reasonable to conclude that the canal water imports are smaller in magnitude compared to precipitation during the rainy months (July-Sept), representing about 5 to 15% of the monthly precipitation. It follows that the fixed prior uncertainty on this term is a justifiable approximation that 485 does not strongly affect the other water balance estimates.

Finally, we note the interplay between all variables: water balance (P , E , C , and Q), weather, and crop variables. Despite relying on external water supplies, the basin has been experiencing a decreasing trend in the river discharge (Dwivedi and Yadav, 2025), coupled with increased posterior evaporation mean from 2010 to 2022 (see the annual timeseries of the posterior mean in Fig. C2). The increase in posterior mean evaporation mirrors the increasing trend in the sugarcane yield and the leaf area index from 2011 (Fig. C4). This aligns with a period of increasing temperatures (see Fig. C4) and with the period when farmers started adopting new high-yielding sugarcane varieties in the basin, as reported by Indian Council of Agricultural Research. The accelerating rate of evaporation in our estimates follows a similar trend in the Landsat-based SSEBop evaporation data set (Fig. C2). This shows, on the one hand, the usefulness of the water balance constraints in evaluating the data products, and on the other hand, that simplified ET models like SSEBop can sufficiently reproduce the evaporation 495 dynamics.

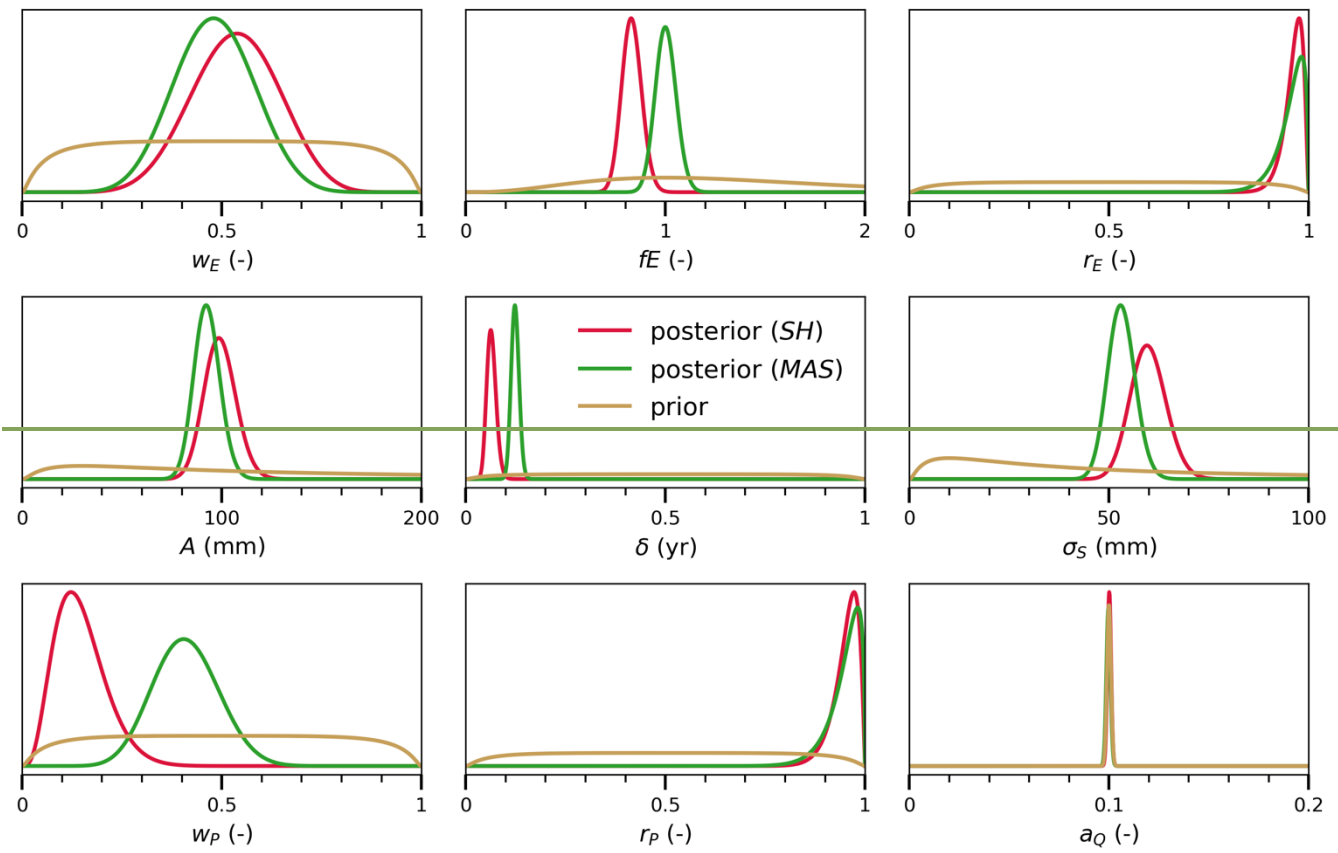
The interplay is also pronounced in dry years such as 2009 and 2016, showing a decline in the posterior mean precipitation, together with the canal water imports. The limited availability of rainfall and surface water for irrigation during droughts, along with rising temperatures in recent years (Fig. C4), does not, however, depress the evaporation rates because crop water demand is met by increased groundwater pumping. The canal water imports is an order of magnitude smaller than evaporation, which also implies dependence on groundwater abstractions. The effect of unsustainable groundwater pumping is particularly 500 notable in the dynamics and trend of basin water storage, which we discuss next.

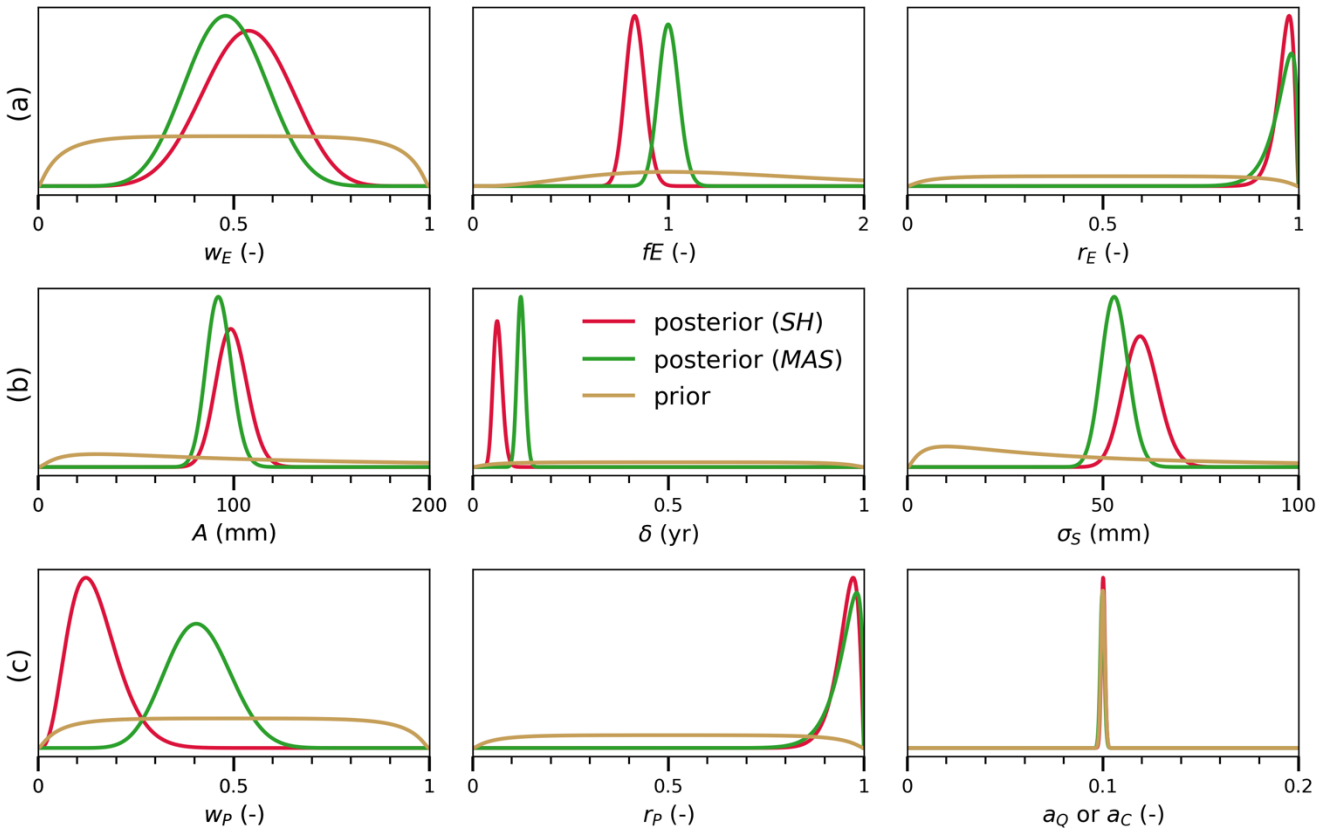




505

Figure 23: Monthly water balance posteriors (90% credible intervals in green) for: (a) P (precipitation), (b) E (actual evapotranspiration), and (c) C (canal water imports), and their corresponding observations (dots). Reference evapotranspiration computed here using ERA5 meteorological input variables is shown as (ET_0). The overbars of the labels in P and E plots indicate that these values are obtained through spatial averaging of the gridded data sets for each month t . Each year's label indicates the start of the year (January).



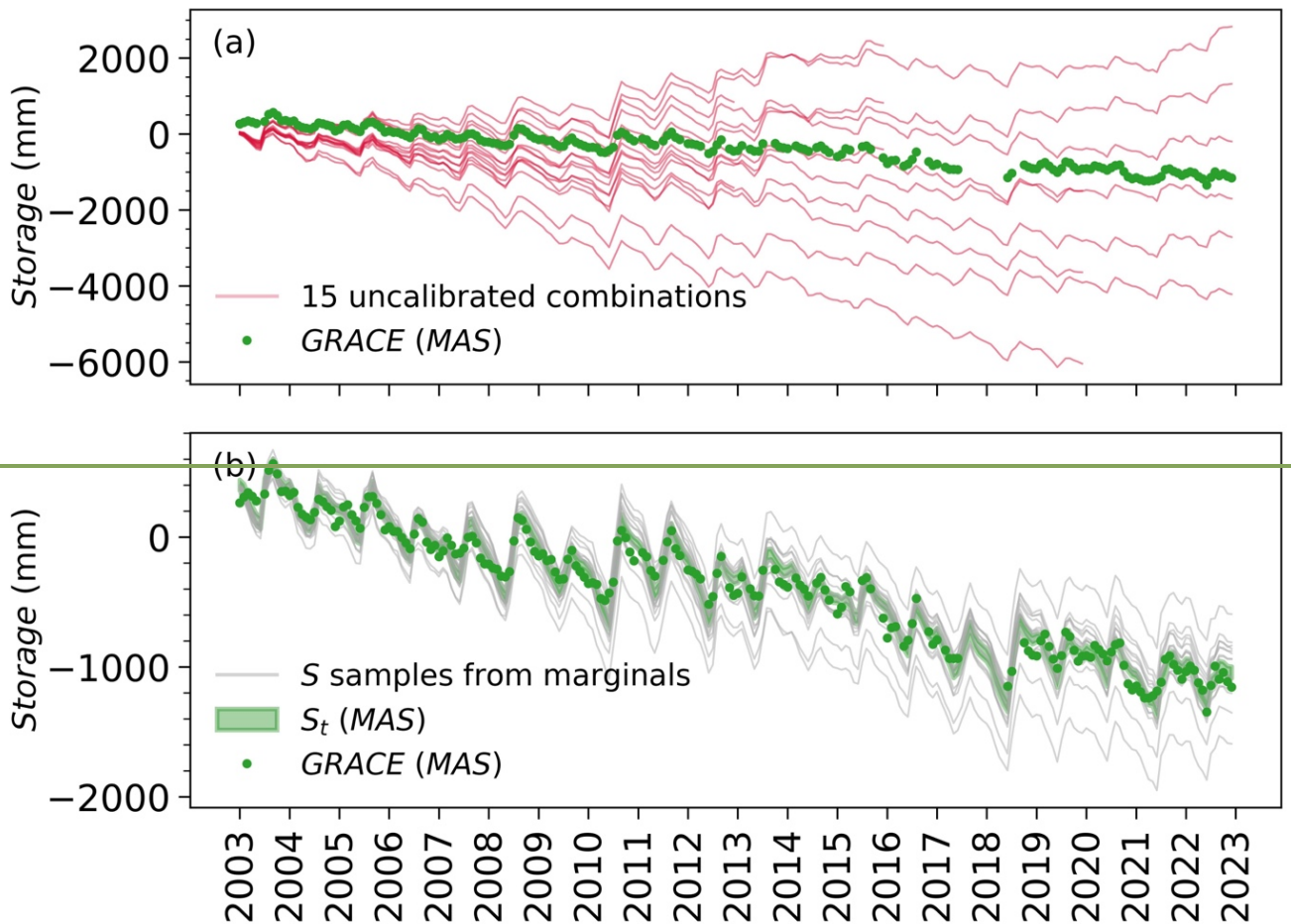


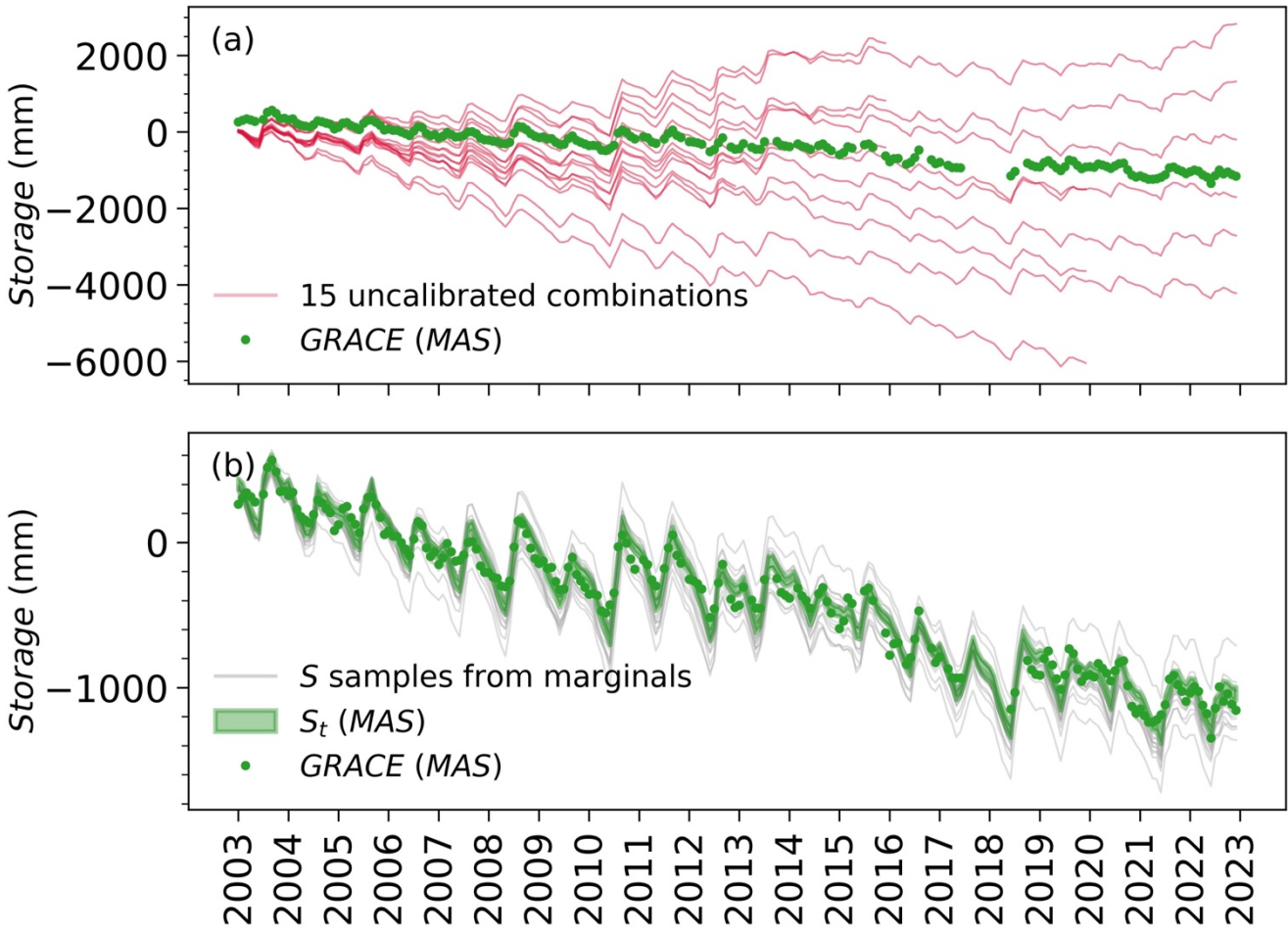
515 **Figure 34:** Prior and posterior distributions of error parameters for: (a) evaporation, (b) storage, (c) precipitation, canal water import, and river discharge when using the range-based P and E prior error model with different GRACE storage data sets: CSR Spherical Harmonic (SH) and JPL Mascon (MAS) solutions.

520 Figure 4-5 compares prior (GRACE data) and posterior estimates of the basin's water storage S . The prior estimates in the top panel are obtained by predicting water storage from the water balance using the original, uncalibrated data sets for P , E , C , and Q . The different permutations in which these data can be combined results in 15 predicted water storage time series in Fig. 4a-5a. We see that the GRACE data closely follow the seasonal dynamics of the prior predicted storages from water balance data. This conveys that both timeseries are approximately in phase but markedly different in magnitude and trend, due to bias and noise in each data set. As shown next, water balance data fusion combines all the data and corrects data errors to yield a closing water balance in each month.

525 The second panel of Fig. 4-5 depicts the calibrated storages, i.e., posteriors shown in green, after fusing all sources of information available on this variable. These posteriors combine three noisy and biased sources of information for storage S in a given month: the GRACE observation (if available for that month), the water balance constraint for the current month, and the water balance constraint for the next month (since S is initial storage for the next month). Fusing all information together results in a narrower storage posterior (with less uncertainty) compared to the individual sources.

In this process, the introduced water balance constraints can themselves significantly contribute to reducing the posterior uncertainty of the inferred storage by inducing correlations between variables. This occurs because (noisily) observing S in this constraint linearly links all the a priori independent variables together. Such a relation is encoded in the coefficients of the variables in the water balance equation. For example, to maintain this physical relation, that is, S remains equal to $S_0 + \bar{P} - \bar{E} - Q + C$, the water balance variables with opposite signs must covary together, and vice versa. Accounting for positive correlations between the variables of opposite signs and negative correlations between the variables with the same signs in the water balance can significantly reduce the variance of S . The effect of these posterior cross-correlations between water balance variables is shown in Fig. 4b 5b. Note the smaller uncertainty in the final posterior estimates (green band), which account for posterior cross-correlations between the variables, compared to posterior samples (in grey) that do not account for these posterior cross-correlations (i.e., by independently sampling from the marginal posteriors of \bar{P} , \bar{E} , Q , and C).





540 **Figure 45:** Monthly timeseries of GRACE-JPL Mascon observations and storage anomalies predicted from the water balance: (a) using 15 unique uncalibrated combinations of the input variables (S_0, P, E, Q, C), and (b) using posterior (calibrated) estimates of the input variables (S_0, P, E, Q, C) with (green band) and without (gray lines) accounting for posterior cross-correlation between the input variables.

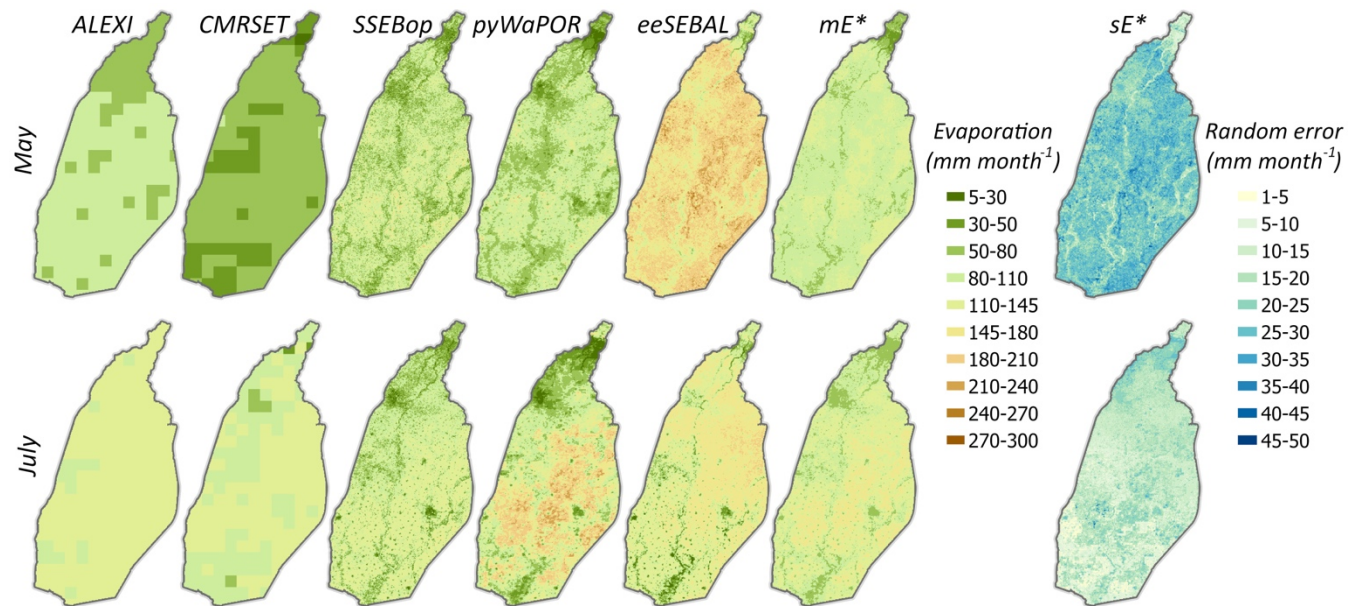
545 **5.2 Grid-scale posteriors**

While grid-scale posteriors of P and E are obtained in each month, we present here detailed results for two months, which were chosen based on previous analysis (Mourad et al., 2024), namely (a) May 2009, representing a dry month before the monsoon with the highest air temperature and with significant differences between evaporation data products, and (b) July 2009, representing the peak rainy month with large differences between precipitation data products. To guide the interpretation of the spatially distributed posteriors, we appended the land use map (see fig. A1).

550 The evaporation maps in Fig. 5-6 show that the posterior mean (mE^*) follows the evaporation estimates available from the diverse range of the original gridded data products. For example, in May, the smallest spatial difference between the posterior evaporation mean and the observed evaporation over the irrigated croplands can be seen by SSEBop, with spatial locations for

these land use elements having values higher or lower than the posterior mean by $\pm 25 \text{ mm month}^{-1}$ (Fig. C4 in Appendix C).

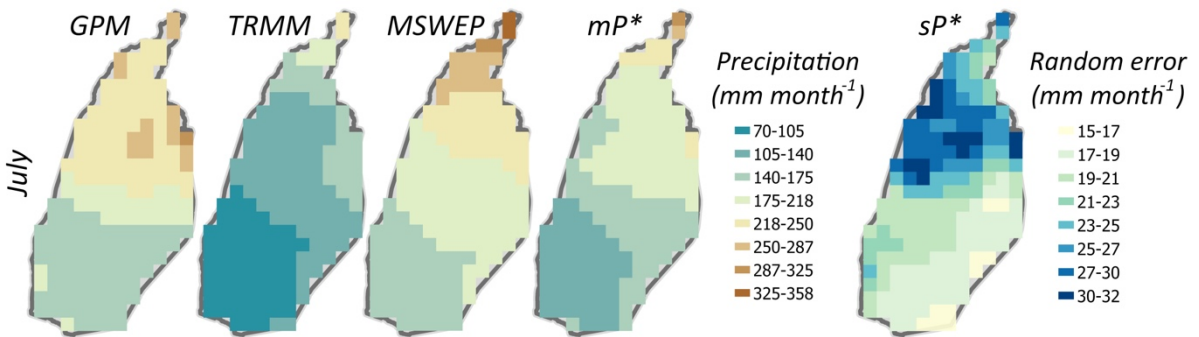
555 Over non-crop lands (urban areas and water bodies), the posterior mean has a better agreement with ALEXI and CMRSET, with differences ranging between -25 and 25 mm month^{-1} . In July, SSEBop displayed the closest agreement with the posterior mean over almost all land use elements. The posterior mean also follows eeSEBAL observed evaporation estimates over irrigated croplands in the lower parts of the basin for this particular month. It is reassuring to see that the generated grid-scale posterior ensemble mean preserves the spatial patterns inherent in the data while combining evaporation information from all
560 products across the different land use elements. This makes sense since the posterior mean is modeled as a weighted average of the minimum and maximum estimates at each grid cell, so that spatial patterns in the original data are maintained. In parallel, the Kalman gain in Eq. (34-30) distributes the basin-wide constraints to the individual E pixels by explicitly accounting for spatial autocorrelations encoded in the grid-scale covariance matrix (V_{Et}). The results in Fig. 5-6 also indicate that the posterior uncertainty (sE^*) is smaller in the monsoon month (July) than in the dry month (May). This is expected as the data are in better
565 agreement in the peak rainy month than in the dry month. Generally, posterior uncertainty is larger in areas with higher evaporation values (irrigated crop-lands), while non-cropland has both lower evaporation and smaller posterior uncertainty. As such, it can be safely concluded that the spatially distributed calibrated evaporation provides reasonable estimates with acceptable uncertainties that vary with the evaporation magnitude estimated at each pixel.



570 **Figure 5-6: Prior observations and estimated posteriors of grid-scale evaporation E before the monsoon (May 2009) and for a peak rainy month (July 2009); mE^* and sE^* denote the posterior mean and standard deviation of evaporation.**

In Fig. 6-7, we see that the precipitation posterior mean falls between the gridded precipitation data products. The spatial difference maps between the grid-scale observations and the posterior mean show that TRMM observes lower precipitation
575 (by -60 to $-35 \text{ mm month}^{-1}$), while MSWEP observes higher precipitation (by 25 to 48 mm month^{-1}) than the posterior mean.

On the other hand, GPM deviates by -21 to 60 mm month $^{-1}$ from the posterior mean (Fig. C5 in Appendix C). As we have seen with the evaporation standard errors, the grid-scale posterior standard errors of precipitation are the highest at spatial locations where the difference across the products is the largest (upper part of the basin), and vice versa.



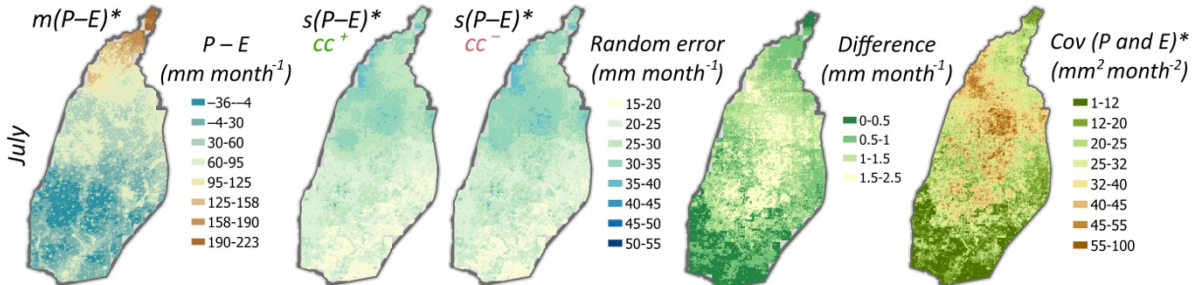
580 **Figure 6.7:** Prior observations and estimated posteriors of grid-scale precipitation P for the peak rainy month (July 2009); mP^* and sP^* denote the posterior mean and standard deviation of precipitation.

Via Eq. (30.29), the posterior cross-correlation between water variables at the basin scale is propagated to the grid scale, and thus results in posterior cross-correlation between grid-scale P and E as well. The effect of this can be illustrated by computing

585 derived variables that involve both P and E . An example is given in Fig. 7.8, which shows maps of the posterior mean and standard deviation of $P - E$ for July 2009, the latter with and without posterior cross-correlation between P and E . Due to positive posterior cross-correlation between P and E (since they have opposite signs in the water balance), the posterior standard deviation of $P - E$ decreases when accounting for this correlation, but the effect in Fig. 7.8 is relatively small, and is observed at some localized spots with the highest reduction in errors of up to 2.5 mm month $^{-1}$. These spots correspond to the 590 locations at which both P and E covary the most, with the cross-covariance subtracted during the computation of the $P - E$ posterior variance. The reason for this relatively small effect is that the water balance constraints introduce other posterior cross-correlations as well, both at the basin scale (Table 2) and at the grid scale via nonlocal posterior cross-correlations between P and E induced by Eq. (30.29) (i.e., in the posterior, P in a grid cell becomes correlated with E in all other grid cells).

To evaluate the effect of ignoring the posterior correlation between P and E , we calculated the distribution of Q from the water 595 balance given the posterior of all other variables for three cases: (i) ignoring all posterior correlation, (ii) ignoring only correlation between P and E , (iii) accounting for all correlation. We compare these distributions to a fourth scenario (iv) in which Q is obtained from uncalibrated water balance data. Writing the water balance (Eq. (1)) in terms of Q results in 15 uncalibrated Q estimates generated from the unique combinations of the water balance data. The distribution for this case is characterized in terms of mean (average across the 15 uncalibrated values) and uncertainty (set as the spread across these 600 values). The results in Fig. 8.9 indicate that neglecting the posterior cross-correlation between P and E and between all water balance variables, can substantially lead to higher uncertainties (wider distributions), compared to when cross-correlations between all variables are accounted for (narrow distribution). At the extreme end, the Q predicted from the uncalibrated water balance data demonstrated the highest level of uncertainty compared to all other cases, with physically inconsistent values

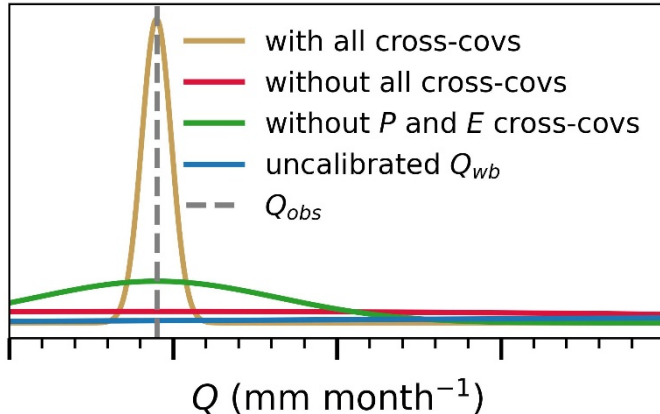
(negative) and a mean value greatly deviating from the observed Q value. We repeat this experiment for all months and report
605 the performance of the estimated Q from the different approaches compared to the observed Q estimates. [The](#) [We obtain a](#) low
RMSE value of the calibrated Q posterior mean ($0.7 \text{ mm month}^{-1}$) compared to Q_{wb} [obtained](#) from uncalibrated water balance
data (74 mm month^{-1}), [which](#) underscores the importance of (i) water balance data fusion for bias-correcting the original data
products and (ii) accounting for posterior correlation, when water balance variables (P, E, C, S) are to be used for computing
 Q .



610 | Figure 78: Grid-scale posterior mean m_{P-E}^* and standard deviation s_{P-E}^* of $P - E$, and P and E covariance for July 2009. The
posterior standard deviations are computed for the two cases: with (cc^+) and without (cc^-) accounting for posterior cross-
correlations (cc) between P and E , while the difference $cc^- - cc^+$ between these two cases illustrates the impact of accounting for
cross-correlations.

615 | Table 2: Basin-scale posterior covariance matrix of all water balance variables for July 2009, the diagonal elements represent the
posterior variances (mm month^{-1}) ([shown in bold](#)), while the off-diagonal entries represent the posterior covariances between the
variables ($\text{mm}^2 \text{ month}^{-2}$) ([underlined values](#)).

	S_{t-1}	\bar{P}	\bar{E}	Q	C
S_{t-1}	562	<u>-255</u>	<u>62</u>	<u>5</u>	<u>-9</u>
\bar{P}	<u>-255</u>	499	<u>49</u>	<u>4</u>	<u>-7</u>
\bar{E}	<u>62</u>	<u>49</u>	158	<u>-1</u>	<u>2</u>
Q	<u>5</u>	<u>4</u>	<u>-1</u>	14	<u>0.1</u>
C	<u>-9</u>	<u>-7</u>	<u>2</u>	<u>0.1</u>	23



620 **Figure 9:** Distribution of Q in comparison to the observed Q_{obs} value (July 2009), for the following cases: (i) ignoring and accounting for posterior correlations between all water balance variables, (ii) ignoring only posterior correlation between P and E , and (iii) Q_{wb} obtained from uncalibrated water balance data. The labels and tick marks are not shown due to data sharing restrictions.

625 6 Discussion

This section evaluates some of the modeling decisions and their impact on the results, specifically the choice of GRACE data set and the choice of spatial correlation lengths of P and E .

6.1 Water balance data fusion with different GRACE data

630 The Hindon basin studied here is experiencing groundwater depletion (Alam and Umar, 2013). Storage data from GRACE satellite has been used to estimate human-driven water storage changes, such as those caused by intensive irrigation. This data is either based on spherical harmonic coefficients or mascon basis function, which entails testing the sensitivity of the water balance closure to the chosen GRACE input. The baseline results presented in Sect. 5 are based on GRACE-JPL Mascon (MAS) solution. Here, we compare these ~~closure~~ results to those obtained using the CSR spherical harmonic (SH) solution.

635 Figure 9–10 compares the posterior distributions for storage and error parameters from both data sets. The corresponding error parameter posteriors are compared in Fig. 34. The two products show negative depleting trends with widely varying magnitudes of $-43.3 \text{ mm year}^{-1}$ from the SH and $-88.7 \text{ mm year}^{-1}$ from MAS. Looking at their corresponding posterior distributions, we can see that they both largely follow the GRACE data, but with an increase in the seasonal amplitude compared to the data. This is reflected in the inferred A parameter (row 2 in Fig. 34), with an estimated value of 90–100 mm for both cases. The storage posteriors, thus, restore the seasonal signal amplitude, which tends to be more severely attenuated in small-sized basins like the Hindon basin. Additionally, the other storage error parameters (phase δ and noise σ_s) distributions are well constrained compared to their vague prior distributions. A relatively small phase error (time lag) is obtained using the two data sets. However, the JPL-MAS data yields a smaller noise (53 mm) than the CSR-SH (60 mm) data. The fact that these error parameters are time-invariant and that the posteriors are computed using data from all months via

iterative smoothing allows the probabilistic water balance model to fill in the data gaps present in GRACE data sets from 2011

645

onwards.

Figure 3-4 also depicts the posterior distribution of the precipitation and evaporation error parameters for the two scenarios.

The water balance data fusion run with the CSR spherical harmonic (SH) solution gives more weight to the lower precipitation and evaporation estimates. This is translated into the w_p value of 0.15. Despite that, the posterior evaporation mean lay between the data limits ($w_E=0.5$) for this case, the bias scaling factor (f_E) masked out its effect (with estimated values smaller than 1),

650

pushing the E posterior towards the lower evaporation end (i.e., the baseline evaporation limit). Figure C6 in Appendix C contains the detailed posterior plots for the water balance variables using the GRACE-SH data sets. Apparently, the GRACE-

SH data set's storage dynamics don't match the other water balance variables in terms of water balance closure, at least with the applied P and E ~~range-based~~ error models. Due to the smaller decreasing trend in the GRACE-SH storage data, the inferred evaporation estimates are on average about ~~**~~15% lower than the estimates obtained with the GRACE-MAS data.

655

To consistently compare the data fit from both solutions, we normalize the likelihood by the number of observations in each data set. Consequently, the water balance model with GRACE-MAS data has a slightly larger likelihood (-5.76) than that with GRACE-SH (likelihood -6.0).

This analysis suggests that long-term groundwater depletion in the basin is possibly better captured by the (more severely declining) mascon data, which has important ramifications for the sustainability of irrigation practices in the basin. This

660

conclusion, however, requires further verification with groundwater level trends from piezometer data.

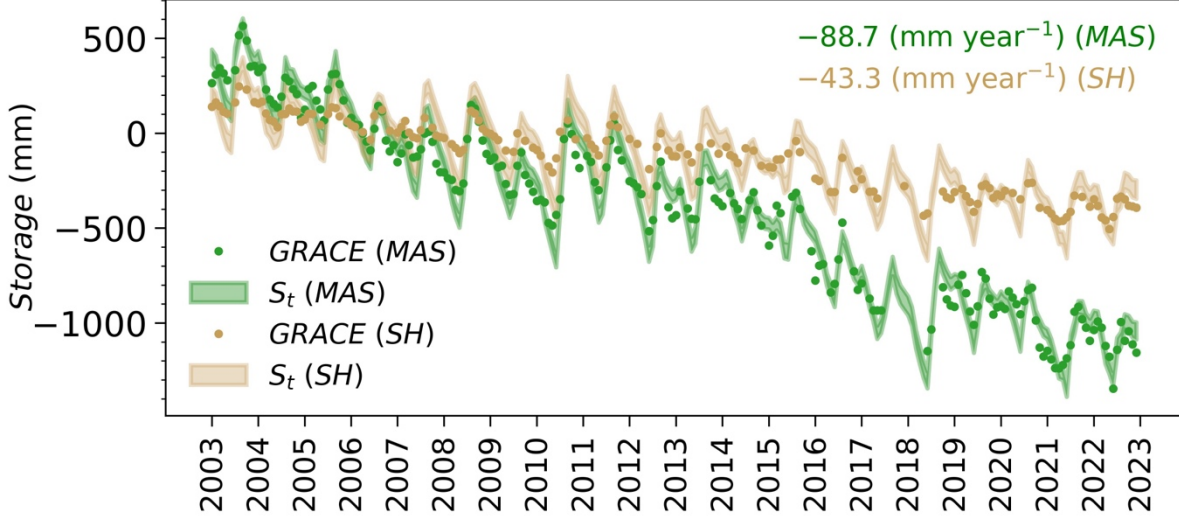


Figure 9-10: Storage posteriors for two different GRACE data sets: GRACE-JPL Mascon (MAS) and CSR spherical harmonic (SH) solution.

6.2 Sensitivity to the assumed spatial correlation length-scale parameters

665 The posterior results in the preceding section are obtained by running the water balance data fusion with fixed Matérn parameters for both the evaporation and precipitation processes. Given the differences in spatial resolution of the analyzed data, the smoothness and correlation length-scale l_s were specified with mid-range values of 1.5 and 50 km, respectively. To evaluate the sensitivity of the results to the chosen value for l_s , we set the value of precipitation l_s at 50 km and vary that of evaporation, and vice versa. Table 3 lists these prior conditions, along with the likelihood and average posterior standard deviation for each water balance variable. The results show stability of the posteriors and the likelihood values under all prior settings, except for the cases where precipitation and evaporation l_s are low (e.g., 20 km). In these cases, the probabilistic water balance exhibits the poorest fit to the data (i.e., small likelihood values), and the basin-scale posterior uncertainty of either evaporation or precipitation tends to be underestimated. On the other hand, using mid-range to larger spatial correlation length scale values produces slightly different but substantively comparable posteriors and likelihood values. The relative 670 insensitivity to l_s suggests its value could potentially be chosen to a very large value to speed up the computations: in the limit of perfect spatial correlation, the formulas linking grid and basin scales simplify, which can result in much faster computations for large grids.

680 **Table 3: Average posterior standard deviation (mm month⁻¹) for each water balance variable and likelihood values under different spatial correlation length-scale (l_s) prior settings. The bold and underlined values represent the results of the baseline setup of the water balance data fusion model, with GRACE-JPL Mascon data set and fixed correlation length scale at 50 km.**

Spatial correlation length-scale (l_s) prior settings (km)		Likelihood	Average posterior standard deviation (mm month ⁻¹)				
			<i>S</i>	<i>P</i>	<i>E</i>	<i>Q</i>	<i>C</i>
20	50	-1207.58	20.1	6.7	6.7	1.8	4.4
30	50	-1198.62	20.5	6.7	8.4	1.8	4.5
40	50	-1193.68	20.8	6.7	9.4	1.8	4.5
50	50	-1191.66	21.3	6.8	10.2	1.8	4.4
60	50	-1245.32	24.8	6.4	10.6	1.8	4.5
70	50	-1188.22	21.3	6.5	10.7	1.8	4.5
80	50	-1190.69	21.1	5.8	11.1	1.8	4.5
90	50	-1190.37	21.6	6.0	11.5	1.8	4.5

6.3 Sensitivity of the posteriors to the prior canal water import estimates

The baseline results presented in Sect. 5.1 are based on the canal water import data generated using ~~ta combination of canal design capacities multiplied by their operational time, and the data average of years with similar conditions (he approach described in Appendix A-2 (Sect. A2)~~. Here, we evaluate the sensitivity of the probabilistic water balance model to the different

685 approaches used to generate canal water estimates from little available data, compared to the one adopted in the baseline run
 (we refer to it here as scenario 1). To do so, we include two additional scenarios, one in which the prior canal estimates are
 computed ~~as using only~~ the canal design capacities multiplied by their operational time obtained from irrigation schedules
 (scenario 2), and the other is based on the assumption that the total flows into the basin are 20% of the monthly flows in the
 690 UGC main canal (scenario 3). For this evaluation, we assess the model fit given the data (likelihood value) and the average
 posterior standard deviation (mm month^{-1}) for each water balance variable. The resulting water balance variables posteriors
 showed minimal variations with the different water supplies prior estimates (Table 4). Although the fit is better with scenarios
 2 and 3, the posterior error for this term is the lowest for scenario 1. Generally, this analysis shows an insensitivity of water
 balance posteriors to the canal water data used, and indicates that the prior estimates presented in Sect. 5.1 are sufficient for
 the goal of constraining the other water balance variables.

695 **Table 4: Average posterior standard deviation (mm month^{-1}) for each water balance variable and likelihood values with different
 canal water import prior estimates. The bold and underlined values represent the results of the baseline setup of the water balance
 data fusion model, with GRACE-JPL Mascon data set and fixed correlation length scale at 50 km.**

scenario	Likelihood	Average posterior standard deviation (mm month^{-1})				
		<i>S</i>	<i>P</i>	<i>E</i>	<i>Q</i>	<i>C</i>
1	<u>-1191.66</u>	<u>21.3</u>	<u>6.8</u>	<u>10.2</u>	<u>1.8</u>	<u>4.4</u>
2	-1174.55	20.7	6.4	9.8	1.8	5.3
3	-1171.91	21.0	6.6	10.0	1.8	5.2

6.4 Extensions

700 The presented methodology is motivated by the availability of diverse water balance remote sensing data, with very few in
 situ data available for the Hindon basin, making independent validation of our estimates challenging. For this reason, we
 evaluated our results using soft validation techniques. For example, for evaporation, in the absence of in situ data, we
 compared the trend in our estimated evaporation with independent crop yield data, and the seasonal dynamics with known
 cropping and irrigation patterns (see Sect. 5.1). As for the precipitation posterior estimates, in Sect. 5.1 and Appendix C, these
 were compared to the spatially interpolated rain gauge dataset for the basin from the Indian Meteorological Department (IMD),
 705 keeping in mind the potential underestimation of precipitation by this dataset (Goteti and Famiglietti, 2024). Evaluating the
 total water storage estimates with independent data is more challenging. In a follow-up study, we will introduce separate
 rootzone and groundwater balance constraints, with the aim of estimating their contributions to the total water balance. At that
 point, it will become possible to use available remote sensing soil moisture data, as well as in-situ groundwater level data, for
 evaluation. Furthermore, adding these additional constraints and data will allow for updating the posterior estimates in this
 710 paper.

Additionally, the presented methodology is general and can be applied to other gauged river basins. For example, an application
 to multiple semi-arid basins was reported in Schoups and Nasseri (2021). The method has several advantages that allow this,

715 including the straightforward and flexible implementation, as it consists of two separate parts: error models specification for each water balance variable that can be customized to fit specific settings, and the model solver that automatically computes the posterior distributions. In addition, the method is set up to rely on in situ and satellite data that inherently capture the hydrological processes. For example, the precipitation data sets estimate the precipitation phase (snow and rain), while evaporation data sets can be used to differentiate between the different land use classes. However, in snow-dominant basins where precipitation data sets might underrepresent this process, or in urban-dominant settings where coarse-resolution evaporation data products might overestimate evaporation, it may be valuable to tailor the error models to local conditions in 720 order to improve the results. Perhaps, this could be achieved by complementing the precipitation error models with other satellite data sets, like the snow cover, snow depth, or temperature products, for better snow detection and mapping. Moreover, evaporation error models can be complemented with land use maps while also considering the use of high-resolution evaporation products or other data sets with improved evaporation estimates of heterogeneous urban surfaces. The major 725 assumption here is that formulating the error models by exploiting ancillary information would allow it to solve for error parameters and water balance variables under varying climatic zones and settings. Alternatively, for this purpose, we could combine the data error models with hydrological models that explicitly account for detailed processes and differentiate between the different hydrological responses.

730 7 Conclusions

This paper presents a multi-scale monthly probabilistic water balance data fusion model for calibrating estimates of each component of the water balance. A key contribution of this paper is the calibration of gridded precipitation and evaporation estimates in an ensemble approach that fully exploits the prior information content of the data. To achieve this, the introduced methodology is applied at two scales: the basin scale and the grid scale. First, we formulate prior grid-scale and ensemble-based error models for precipitation and evaporation with unknown error parameters that describe the bias and random errors in their spatial fields. The spatially averaged inputs to the precipitation and evaporation error models, along with in situ data (river discharge and canal imports) and storage data from GRACE, then drive a basin-scale probabilistic water balance closure approach. In this approach, the water balance is treated as a Bayesian model by assigning prior distributions with unknown bias and noise parameters to each water balance variable. Combining these prior distributions with monthly water balance 735 constraints results in posterior estimates of all parameters and variables that jointly close the water balance at the basin scale. The resulting basin-scale precipitation and evaporation posteriors and their cross-correlations are then used to update the prior grid-scale data from the first step. This is attained using a Kalman smoothing algorithm that ensures consistency between the grid-scale and the basin-scale estimates; that is, spatially averaging the calibrated gridded estimates yields monthly precipitation and evaporation values that jointly satisfy the water balance at the basin scale together with the other variables 740 745 (C, Q, S).

We apply the introduced methodology to the Hindon Basin, a tributary of the Yamuna River that suffers from unsustainable irrigation practices relying on the local groundwater and imported surface water. The basin-scale results demonstrate that introducing an independent set of in situ data on surface water imports and river discharge, along with monthly water balance constraints, updates the prior information with new information, automatically adjusts different information sources for each 750 water balance variable, while maintaining a closed water balance. The output of this study highlights the potential of the monthly water balance constraints in substantially reducing uncertainties by accounting for cross-correlations between all water balance variables. In addition, the model yields basin-wide posterior estimates of: (a) error parameters that are well constrained by all water balance data, and (b) consistent basin-scale water balance variables that jointly close the water balance. Transferring these basin-scale constraints to the grid scale results in: (a) posterior ensemble mean of precipitation and 755 evaporation that fuses the pixel-wise information from extreme prior data bounds (min-max) and finds a balance between the two according to their relative errors, and (b) posterior random errors that reflect the model confidence about the location of the posterior mean at each grid cell.

Explicit to the introduced approach are the assumptions made about the data to characterize their associated errors in a parametric form. For instance, a range-based error model is used to quantify errors in the gridded precipitation and evaporation 760 data. Here, the bias error is described as a weighted average of the minimum and maximum estimates at each spatial location. Whereas, the random error is quantified by scaling the maximum potential error (i.e., scaling one-quarter of the grid-scale full range). As an extension to this analysis, alternative data error models might be worth considering. E.g., a possible alternative is to use Gaussian mixture models that calibrate each data set individually, while still exploiting the water balance as a constraint.

765 As for the errors in a single GRACE data set, these are modeled using a noisy sine wave error model with unknown phase and amplitude error parameters that are used to correct for the dominant biases in the GRACE data (i.e., leakages). The sensitivity of the model results to the input data is assessed using two GRACE data sets: spherical harmonic (GRACE-CSR) and mascon solution (GRACE-JPL). This is done quantitatively by comparing the values of the inferred noise parameters (a smaller value is preferred) and that of the likelihood, as a larger likelihood corresponds to a better fit. While the GRACE-JPL demonstrated 770 a better performance than GRACE-CSR based on these evaluation criteria, this could also be influenced by the assumptions surrounding the precipitation and evaporation error models. Ground-based piezometer data may also help resolve the difference between the downward trends in the two GRACE data sets for the studied basin, which is important for evaluating the sustainability of irrigation practices in the basin.

Finally, the random errors in the monthly river discharge and canal water import data are more or less fixed to relative errors. 775 A larger prior uncertainty is assigned to the gap-filled canal import data (25%) than to the river discharge (10%). Regardless of the approach used to generate prior canal water import estimates from little available data, these were sufficient to constrain the other water balance terms. Additionally, the generated water balance estimates are not strongly affected by the assumed errors for the canal water and river discharge data, as these two variables are relatively small compared to the other monthly water balance variables (especially during rainy months when the two processes are driven by precipitation). We also examined

780 the impact of fixing the spatial correlation length scale parameter on model fit and the posterior standard errors. The posterior results showed robustness and model fit improvement across mid-to-large values of prior parameter sets. This suggests that this parameter does not influence the model results in a large way.

785 A key aspect of the proposed methodology is that it is data-driven, exploiting the water balance constraint as an independent source of information. Therefore, the resulting calibrated data generated here can be used as baseline data sets for multiple applications, such as the validation or calibration of hydrological models, climate studies, and water accounting assessments.

790 Nonetheless, updating the calibrated and spatially distributed estimates of precipitation and evaporation, and storage data generated herein with constraints describing the physical relations between detailed water balance variables (e.g., vertical and horizontal flows), along with additional in situ data (e.g., groundwater storage observations from piezometers), hold a great premise for synergetic and complementary use of all information sources. This will be the scope of a follow-up study for the investigated basin that aims to constrain water balance stocks and flows and their errors ~~within a water accounting tool that using enforces~~ grid-scale water balance constraints (Hessels et al., 2022).

Code and data availability

795 All software used to collect the data is available at <https://doi.org/10.5281/zenodo.11148992>
<https://doi.org/10.5281/zenodo.11148992>. The source code developed for this research is available via:
<http://doi.org.tudelft.idm.ecl.ele.org/10.5281/zenodo.4116451>. <https://zenodo.org/records/17348274>.

Author contributions

RM: methodology, software, formal analysis, validation, visualisation, writing original draft, writing (review & editing). GS: conceptualization, methodology, software, formal analysis, validation, writing (review & editing), supervision, funding acquisition. VR: data provision, review. WB: funding acquisition, review.

800 Competing interests

The contact author has declared that none of the authors has any competing interests.

Acknowledgments

805 The authors would like to thank Bas Mohrmann for coordinating and facilitating access to the river discharge and canal water import data used in this study. Also, the authors thank Ankur Rohel, Dikshant Bodana, Vivek Tiwari, and M. Sai Bargav Reddy for helping with canal water data access and entry.

Financial support

This work is supported by the Dutch Research Council, Government of The Netherlands, through the Meridian Fund (project no. 482.20.303) and by the Department of Science & Technology, Government of India (project no. DST/TMDEWO/WTI/NWO/CGAW/2020/14), under the jointly funded Cleaning the Ganga and Agri-Water initiative and the Hindon Roots Sensing (HIROS) project: River Rejuvenation through Scalable Water- and Solute Balance Modelling and Informed Farmers' Actions.

References

Abatzoglou, J. T., Dobrowski, S. Z., Parks, S. A., and Hegewisch, K. C.: TerraClimate, a high-resolution global dataset of monthly climate and climatic water balance from 1958–2015, *Scientific data*, 5, 1-12, 2018.

815 Abolafia-Rosenzweig, R., Pan, M., Zeng, J., and Livneh, B.: Remotely sensed ensembles of the terrestrial water budget over major global river basins: An assessment of three closure techniques, *Remote Sensing of Environment*, 252, 112191, 2021. Abramowitz, M. and Stegun, I. A.: *Handbook of mathematical functions with formulas, graphs, and mathematical tables*, US Government printing office1968.

Ahmad, F.: Canal Irrigation: Major Legal Issues, *Journal of the Indian Law Institute*, 33, 589-613, 1991.

820 Aires, F.: Combining datasets of satellite-retrieved products. Part I: Methodology and water budget closure, *Journal of Hydrometeorology*, 15, 1677-1691, 2014.

Alam, F. and Umar, R.: Groundwater flow modelling of Hindon-Yamuna interfluve region, western Uttar Pradesh, *Journal of the Geological Society of India*, 82, 80-90, 2013.

825 Anderson, M. C., Norman, J. M., Mecikalski, J. R., Otkin, J. A., and Kustas, W. P.: A climatological study of evapotranspiration and moisture stress across the continental United States based on thermal remote sensing: 2. Surface moisture climatology, *Journal of Geophysical Research: Atmospheres*, 112, 2007.

Anderson, M. C., Zolin, C. A., Hain, C. R., Semmens, K., Yilmaz, M. T., and Gao, F.: Comparison of satellite-derived LAI and precipitation anomalies over Brazil with a thermal infrared-based Evaporative Stress Index for 2003–2013, *Journal of Hydrology*, 526, 287-302, 2015.

830 Barkhordari, H., Dastjerdi, P. A., and Nasseri, M.: Development of a framework estimating regional gridded streamflow and actual evapotranspiration datasets: Fusing Budyko and water balance closure methods using remotely sensed ancillary data, *Journal of Hydrology*, 133456, 2025.

Bastiaanssen, W., Cheema, M., Immerzeel, W., Miltenburg, I., and Pelgrum, H.: Surface energy balance and actual evapotranspiration of the transboundary Indus Basin estimated from satellite measurements and the ETLook model, *Water Resources Research*, 48, 2012.

835 Bastiaanssen, W. G. M., Hoekman, D. H., and Roebeling, R.: A methodology for the assessment of surface resistance and soil water storage variability at mesoscale based on remote sensing measurements. A case study with HAPEX-EFEDA data, *Landbouwuniversiteit Wageningen*0926-230X, 1993.

Beck, H. E., Wood, E. F., Pan, M., Fisher, C. K., Miralles, D. G., Van Dijk, A. I., McVicar, T. R., and Adler, R. F.: MSWEP V2 global 3-hourly 0.1 precipitation: methodology and quantitative assessment, *Bulletin of the American Meteorological Society*, 100, 473-500, 2019.

Cawse-Nicholson, K., Braverman, A., Kang, E. L., Li, M., Johnson, M., Halverson, G., Anderson, M., Hain, C., Gunson, M., and Hook, S.: Sensitivity and uncertainty quantification for the ECOSTRESS evapotranspiration algorithm–DisALEXI, *International journal of applied earth observation and geoinformation*, 89, 102088, 2020.

845 Central Water Commission: Discahrge data for Galeta Station, Obtained from CWC, Government of India [dataset], 2024. Chaube, U. C., Pandey, A., and Singh, V. P.: *Canal Irrigation Systems in India: Operation, Maintenance, and Management*, Springer Nature2023.

Chen, H., Ding, L., and Tuo, R.: Kernel packet: An exact and scalable algorithm for Gaussian process regression with Matérn correlations, *Journal of machine learning research*, 23, 1-32, 2022.

850 Crosetto, M., Ruiz, J. A. M., and Crippa, B.: Uncertainty propagation in models driven by remotely sensed data, *Remote Sensing of Environment*, 76, 373-385, 2001.

Dwivedi, P. and Yadav, B. K.: Inference of hydrological modelling and field-based monitoring on dynamics of heavy metals in water of Hindon Basin, *Journal of Hydrology: Regional Studies*, 60, 102488, 2025.

Foken, T.: The energy balance closure problem: An overview, *Ecological Applications*, 18, 1351-1367, 2008.

855 Goteti, G. and Famiglietti, J.: Extent of gross underestimation of precipitation in India, *Hydrology and Earth System Sciences Discussions*, 2024, 1-40, 2024.

Guerschman, J. P., Van Dijk, A. I., Mattersdorf, G., Beringer, J., Hutley, L. B., Leuning, R., Pipunic, R. C., and Sherman, B. S.: Scaling of potential evapotranspiration with MODIS data reproduces flux observations and catchment water balance observations across Australia, *Journal of hydrology*, 369, 107-119, 2009.

860 Gumma, M. K., Thenkabail, P. S., Panjala, P., Teluguntla, P., Yamano, T., and Mohammed, I.: Multiple agricultural cropland products of South Asia developed using Landsat-8 30 m and MODIS 250 m data using machine learning on the Google Earth Engine (GEE) cloud and spectral matching techniques (SMTs) in support of food and water security, *GIScience & Remote Sensing*, 59, 1048-1077, 2022.

Handcock, M. S. and Stein, M. L.: A Bayesian analysis of kriging, *Technometrics*, 35, 403-410, 1993.

865 Heberger, M. G., Pellet, V., and Aires, F.: Improving Satellite Remote Sensing Estimates of the Global Terrestrial Hydrologic Cycle via Neural Network Modeling, *Authorea Preprints*, 2023.

Hensman, J., Matthews, A., and Ghahramani, Z.: Scalable variational Gaussian process classification, *Artificial intelligence and statistics*, 351-360,

Hessels, T., Davids, J. C., and Bastiaanssen, W.: Scalable Water Balances from Earth Observations (SWE0): results from 50 years of remote sensing in hydrology, *Water International*, 47, 866-886, 2022.

870 Hobeichi, S., Abramowitz, G., Contractor, S., and Evans, J.: Evaluating precipitation datasets using surface water and energy budget closure, *Journal of Hydrometeorology*, 21, 989-1009, 2020.

Hong, Y., Hsu, K. l., Moradkhani, H., and Sorooshian, S.: Uncertainty quantification of satellite precipitation estimation and Monte Carlo assessment of the error propagation into hydrologic response, *Water resources research*, 42, 2006.

875 Horner, I., Renard, B., Le Coz, J., Branger, F., McMillan, H., and Pierrefeu, G.: Impact of stage measurement errors on streamflow uncertainty, *Water Resources Research*, 54, 1952-1976, 2018.

Hou, A. Y., Kakar, R. K., Neeck, S., Azarbarzin, A. A., Kummerow, C. D., Kojima, M., Oki, R., Nakamura, K., and Iguchi, T.: The global precipitation measurement mission, *Bulletin of the American meteorological Society*, 95, 701-722, 2014.

Huffman, G., Stocker, E., Bolvin, D., Nelkin, E., and Tan, J.: GPM IMERG Final Precipitation L3 1 month 0.1 degree x 0.1 degree V06, Goddard Earth Sciences Data and Information Services Center (GES DISC): Greenbelt, MD, USA, 2019.

880 Huffman, G. J., Bolvin, D. T., Nelkin, E. J., Wolff, D. B., Adler, R. F., Gu, G., Hong, Y., Bowman, K. P., and Stocker, E. F.: The TRMM multisatellite precipitation analysis (TMPA): Quasi-global, multiyear, combined-sensor precipitation estimates at fine scales, *Journal of hydrometeorology*, 8, 38-55, 2007.

Indian Council of Agricultural Research: Indian Council of Agricultural Research, Co 0238 – The Wonder Variety of Sugarcane: <https://icar.org.in/en/node/4869>.

885 International Crops Research Institute for the Semi-Arid Tropics: District Level Database (DLD): Crops dataset, <http://data.icrisat.org/dld/src/crops.html>.

Irrigation & Water Resources Department: Canal discharge data for Hindon River Basin, Obtained from Irrigation & Water Resources Department, Uttar Pradesh, Government of India [dataset], 2024.

890 Joseph, J. and Ghosh, S.: Representing Indian agricultural practices and paddy cultivation in the variable infiltration capacity model, *Water Resources Research*, 59, e2022WR033612, 2023.

Karimi, P., Bastiaanssen, W. G., Molden, D., and Cheema, M. J. M.: Basin-wide water accounting based on remote sensing data: an application for the Indus Basin, *Hydrology and Earth System Sciences*, 17, 2473-2486, 2013.

Kuczera, G.: Correlated rating curve error in flood frequency inference, *Water resources research*, 32, 2119-2127, 1996.

895 L'Ecuyer, T. S. and Stephens, G. L.: An estimation-based precipitation retrieval algorithm for attenuating radars, *Journal of Applied Meteorology and Climatology*, 41, 272-285, 2002.

900 Landerer, F. W. and Swenson, S.: Accuracy of scaled GRACE terrestrial water storage estimates, *Water resources research*, 48, 2012.

Long, D., Longuevergne, L., and Scanlon, B. R.: Uncertainty in evapotranspiration from land surface modeling, remote sensing, and GRACE satellites, *Water Resources Research*, 50, 1131-1151, 2014.

Luo, Z., Li, H., Zhang, S., Wang, L., Wang, S., and Wang, L.: A Novel Two-Step Method for Enforcing Water Budget Closure and an Intercomparison of Budget Closure Correction Methods Based on Satellite Hydrological Products, *Water Resources Research*, 59, e2022WR032176, 2023.

905 Maggioni, V., Massari, C., and Kidd, C.: Errors and uncertainties associated with quasiglobal satellite precipitation products, in: *Precipitation science*, Elsevier, 377-390, 2022.

Massari, C., Crow, W., and Brocca, L.: An assessment of the performance of global rainfall estimates without ground-based observations, *Hydrology and earth system sciences*, 21, 4347-4361, 2017.

McMillan, H., Krueger, T., and Freer, J.: Benchmarking observational uncertainties for hydrology: rainfall, river discharge and water quality, *Hydrological Processes*, 26, 4078-4111, 2012.

910 Mourad, R., Schoups, G., Bastiaanssen, W., and Kumar, D. N.: Expert-based prior uncertainty analysis of gridded water balance components: Application to the irrigated Hindon River Basin, India, *Journal of Hydrology: Regional Studies*, 55, 101935, 2024.

Munier, S., Aires, F., Schlaffer, S., Prigent, C., Papa, F., Maisongrande, P., and Pan, M.: Combining data sets of satellite-retrieved products for basin-scale water balance study: 2. Evaluation on the Mississippi Basin and closure correction model, *Journal of Geophysical Research: Atmospheres*, 119, 12,100-112,116, 2014.

915 Myneni, R., Knyazikhin, Y., and Park, T.: MODIS/Terra Leaf Area Index/FPAR 8-Day L4 Global 500m SIN Grid V061, NASA EOSDIS Land Processes Distributed Active Archive Center (DAAC) data set, MOD15A12H. 061, 2021.

Pai, D., Rajeevan, M., Sreejith, O., Mukhopadhyay, B., and Satbha, N.: Development of a new high spatial resolution (0.25×0.25) long period (1901-2010) daily gridded rainfall data set over India and its comparison with existing data sets over the 920 region, *Mausam*, 65, 1-18, 2014.

Pan, M. and Wood, E. F.: Data assimilation for estimating the terrestrial water budget using a constrained ensemble Kalman filter, *Journal of Hydrometeorology*, 7, 534-547, 2006.

Pan, M., Sahoo, A. K., Troy, T. J., Vinukollu, R. K., Sheffield, J., and Wood, E. F.: Multisource estimation of long-term 925 terrestrial water budget for major global river basins, *Journal of Climate*, 25, 3191-3206, 2012.

Pellet, V., Aires, F., Munier, S., Fernández Prieto, D., Jordá, G., Dorigo, W. A., Polcher, J., and Brocca, L.: Integrating multiple satellite observations into a coherent dataset to monitor the full water cycle—application to the Mediterranean region, *Hydrology and Earth System Sciences*, 23, 465-491, 2019.

Rodell, M., Velicogna, I., and Famiglietti, J. S.: Satellite-based estimates of groundwater depletion in India, *Nature*, 460, 999-1002, 2009.

930 Rodell, M., Beaudoin, H. K., L'ecuyer, T., Olson, W. S., Famiglietti, J. S., Houser, P. R., Adler, R., Bosilovich, M. G., Clayson, C. A., and Chambers, D.: The observed state of the water cycle in the early twenty-first century, *Journal of Climate*, 28, 8289-8318, 2015.

Rodell, M., Houser, P., Jambor, U., Gottschalck, J., Mitchell, K., Meng, C.-J., Arsenault, K., Cosgrove, B., Radakovich, J., and Bosilovich, M.: The global land data assimilation system, *Bulletin of the American Meteorological society*, 85, 381-394, 935 2004.

Sahoo, A. K., Pan, M., Troy, T. J., Vinukollu, R. K., Sheffield, J., and Wood, E. F.: Reconciling the global terrestrial water budget using satellite remote sensing, *Remote Sensing of Environment*, 115, 1850-1865, 2011.

Schoups, G. and Nasseri, M.: GRACEfully closing the water balance: A data-driven probabilistic approach applied to river basins in Iran, *Water Resources Research*, 57, e2020WR029071, 2021.

940 Senay, G. B.: Satellite psychrometric formulation of the Operational Simplified Surface Energy Balance (SSEBop) model for quantifying and mapping evapotranspiration, *Applied Engineering in Agriculture*, 34, 555-566, 2018.

Senay, G. B., Parrish, G. E., Schauer, M., Friedrichs, M., Khand, K., Boiko, O., Kagone, S., Dittmeier, R., Arab, S., and Ji, L.: Improving the Operational Simplified Surface Energy Balance Evapotranspiration Model Using the Forcing and Normalizing Operation, *Remote Sensing*, 15, 260, 2023.

945 Sheffield, J., Wood, E. F., Pan, M., Beck, H., Coccia, G., Serrat-Capdevila, A., and Verbist, K.: Satellite remote sensing for water resources management: Potential for supporting sustainable development in data-poor regions, *Water Resources Research*, 54, 9724-9758, 2018.

Sobol, I. M.: Global sensitivity indices for nonlinear mathematical models and their Monte Carlo estimates, *Mathematics and computers in simulation*, 55, 271-280, 2001.

950 Sun, Q., Miao, C., Duan, Q., Ashouri, H., Sorooshian, S., and Hsu, K. L.: A review of global precipitation data sets: Data sources, estimation, and intercomparisons, *Reviews of Geophysics*, 56, 79-107, 2018.

Sun, Y., Bowman, K. P., Genton, M. G., and Tokay, A.: A Matérn model of the spatial covariance structure of point rain rates, *Stochastic Environmental Research and Risk Assessment*, 29, 411-416, 2015.

955 Swenson, S. and Wahr, J.: Post-processing removal of correlated errors in GRACE data, *Geophysical research letters*, 33, 2006.

Ter Braak, C. J. and Vrugt, J. A.: Differential evolution Markov chain with snooker updater and fewer chains, *Statistics and Computing*, 18, 435-446, 2008.

Tian, Y. and Peters-Lidard, C. D.: A global map of uncertainties in satellite-based precipitation measurements, *Geophysical Research Letters*, 37, 2010.

960 Umar, R., Khan, M. M. A., Ahmed, I., and Ahmed, S.: Implications of Kali-Hindon inter-stream aquifer water balance for groundwater management in western Uttar Pradesh, *Journal of earth system science*, 117, 69-78, 2008.

Wada, Y., Van Beek, L. P., Van Kempen, C. M., Reckman, J. W., Vasak, S., and Bierkens, M. F.: Global depletion of groundwater resources, *Geophysical research letters*, 37, 2010.

965 Wahr, J., Swenson, S., Zlotnicki, V., and Velicogna, I.: Time-variable gravity from GRACE: First results, *Geophysical Research Letters*, 31, 2004.

Yin, G. and Park, J.: The use of triple collocation approach to merge satellite-and model-based terrestrial water storage for flood potential analysis, *Journal of Hydrology*, 603, 127197, 2021.

Zhang, K., Kimball, J. S., and Running, S. W.: A review of remote sensing based actual evapotranspiration estimation, *Wiley interdisciplinary reviews: Water*, 3, 834-853, 2016a.

970 Zhang, Y., Pan, M., and Wood, E. F.: On creating global gridded terrestrial water budget estimates from satellite remote sensing, *Remote sensing and water resources*, 59-78, 2016b.

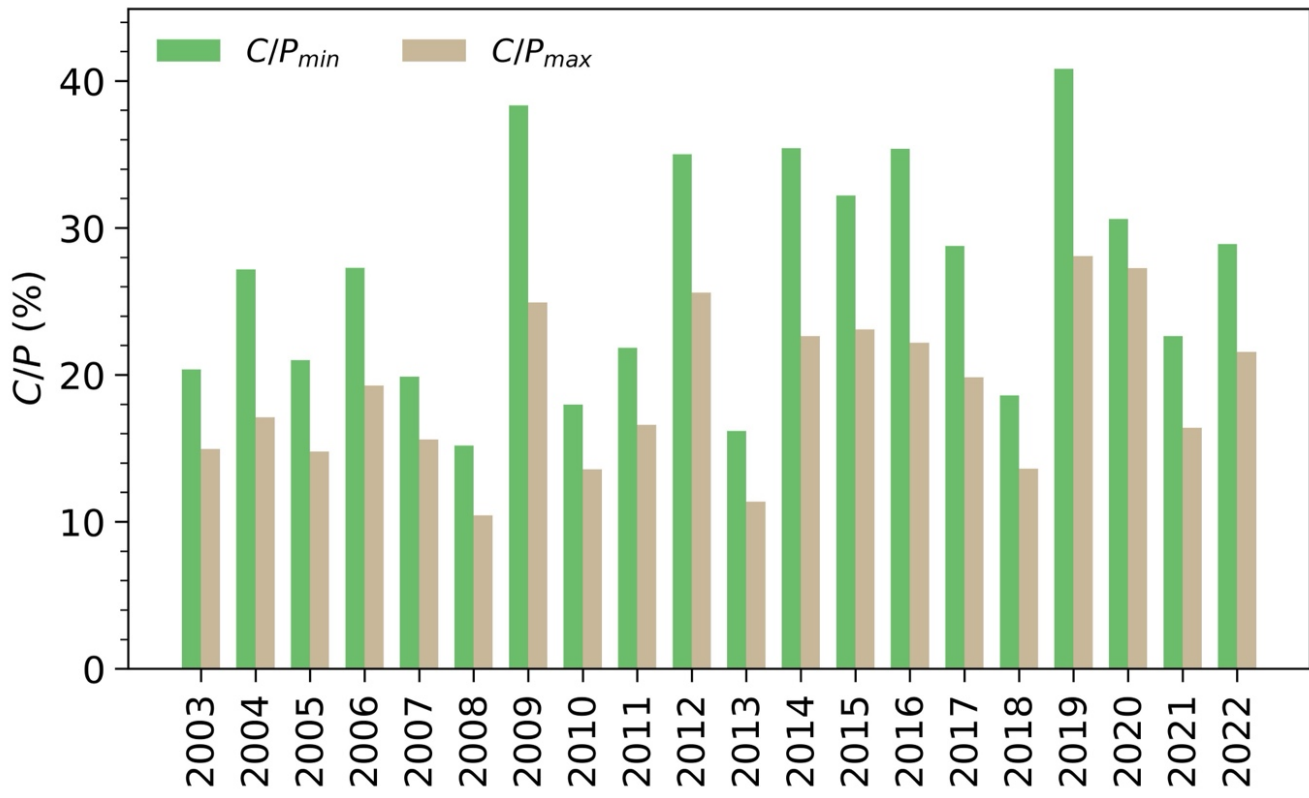
Zhang, Y., Pan, M., Sheffield, J., Siemann, A. L., Fisher, C. K., Liang, M., Beck, H. E., Wanders, N., MacCracken, R. F., and Houser, P. R.: A Climate Data Record (CDR) for the global terrestrial water budget: 1984–2010, *Hydrology and Earth System Sciences*, 22, 241-263, 2018.

975

980

Appendix A

The following subsections summarize the available information on the Hindon basin land use elements (Fig. A1), share of canal water imports in the water balance (Fig. A2), canal network (Figs. A3 and A4), its operation, irrigation canal delivery data, and processing steps.



985

Fig A1: Share of the canal water imports in the water balance, expressed as the percentage of the minimum and maximum remote sensing-based precipitation observations.

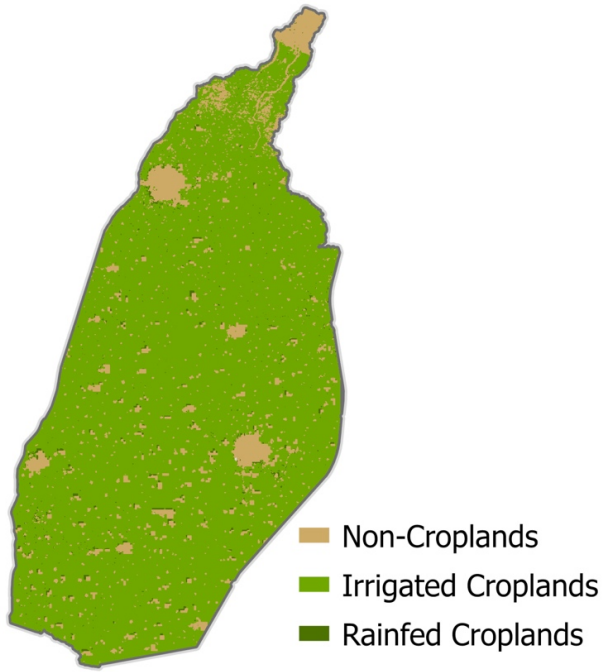


Fig A2: Land use elements distribution in the Hindon basin from Gumma et al. (2022).

990

A1. Description of the canal irrigation system and its operation

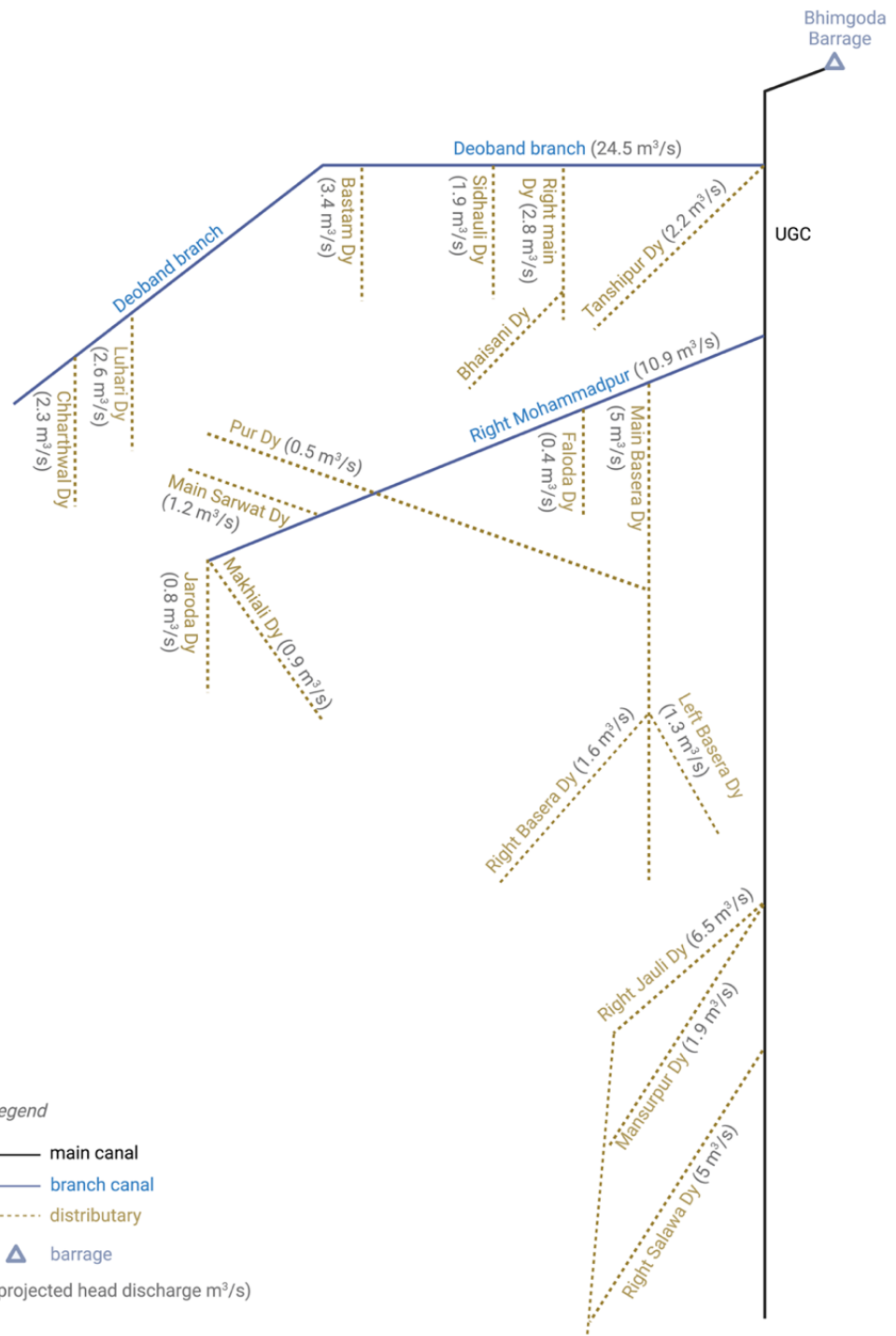
Figs A3 and A4 provide an overview of the canal network's spatial distribution and design capacities. While these main canals run continuously, their distributaries are operated in rotation (Ahmad, 1991; Chaube et al., 2023). The canal distributaries in the Hindon basin are operated on an 'on-off' basis as shown in Table A1. The irrigation schedules (also known as the rosters) are prepared for two irrigational seasons:

995 (1) Kharif season in which the main irrigated crops are sugarcane, rice, cotton, maize, vegetables, and fodder crops
 (2) Rabi season in which the principal crops are wheat, barley, mustard, and peas.

1000 **Table A1: Example of seasonal operational schedule (the ON-OFF basis) for Eastern Yamuna Canal (EYC) and Upper Ganga Canal (UGC) distributaries. Kharif spans from March to September 2021, while Rabi covers Oct 2021 to March 2022.**

Main	Intake	3 weeks ON- 1 week OFF	4 weeks ON	2 weeks ON- 2 weeks OFF	1 week ON- 3 weeks OFF
Canal				OFF	OFF
UGC (Kharif)	Deoband Branch	April,May,July	June,Aug,Sept		
	Tanshipur	July,Aug	June,Sept	April	May
	Mohammadpur	July, Aug	June,Sept	April,May	
	Mansurpur	July,Aug	June,Sept	April,May	

	Deoband Branch	Feb	Nov,Dec,Jan	Oct
UGC	Tanshipur		Nov,Dec,Jan	Feb,Oct
(Rabi)	Mohammadpur		Dec,Jan	Feb,Oct,Nov
	Mansurpur	Dec	Nov, Jan,Feb	Oct
	Nagla	Aug	July	Apr,May,June
	Babail	Aug	July	Apr,May,June
	Sarakadi	Aug	July	Apr,May,June,Sep
EYC	Megh Chappar		June,July,Aug	Apr,Sep
(Kharif)	Chidbana		June,July,Aug	Apr,Sep
	Nalhera	Aug	June	Apr,July,Sep
	Redi	Aug	June	Apr,July,Sep
	Rampuri	Aug	June	Apr,May,July,Sep
	Kallarpur		July,Aug	Apr,May,June,Sep
	Nagla			Oct,Nov,Dec,Jan,Feb
	Babail			Oct,Nov,Dec,Feb
	Sarakadi			Oct,Nov,Dec,Mar
EYC	Megh Chappar			Oct,Nov,Jan,Mar
(Rabi)	Chidbana			Oct,Nov,Jan,Mar
	Nalhera			Oct,Nov,Jan,Mar
	Redi			Oct,Nov,Jan,Mar
	Rampuri			Oct,Dec,Jan,Mar
	Kallarpur			Oct,Dec,Feb



1005 Fig A3: A schematic of the UGC main canal and its distributaries with their respective discharge capacities ($\text{m}^3 \text{ s}^{-1}$).

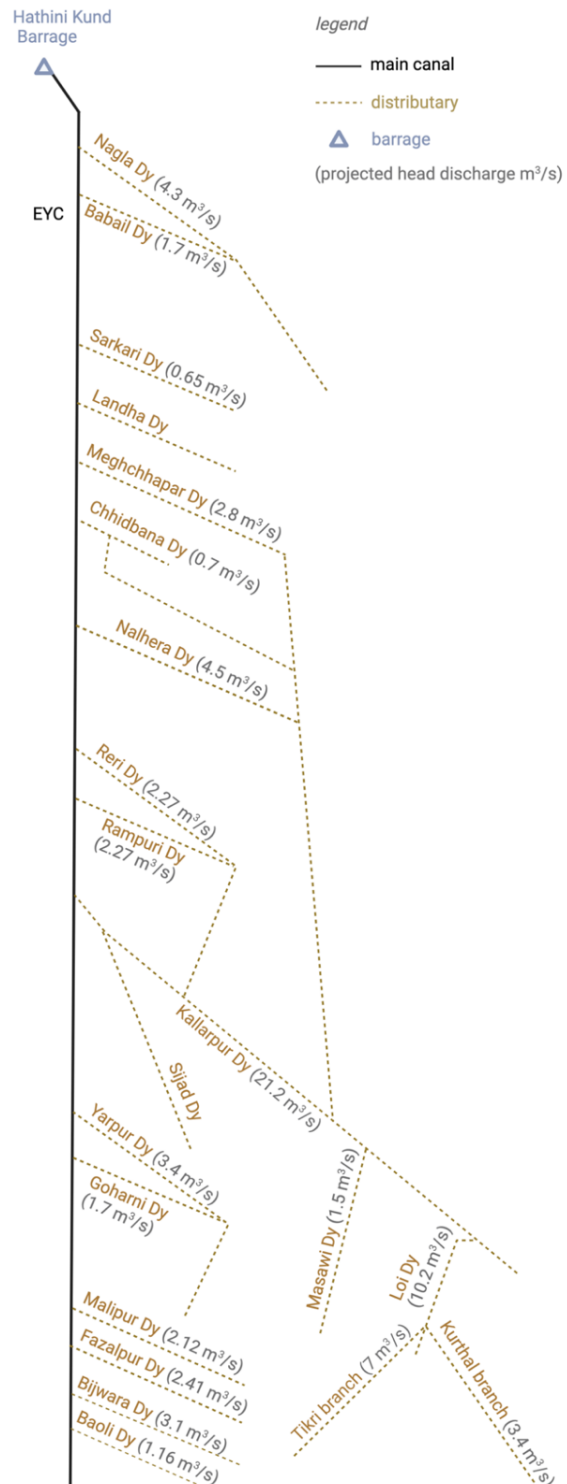


Fig A4: A schematic of the EYC main canal and its distributaries with their respective discharge capacities ($\text{m}^3 \text{ s}^{-1}$).

A2. Description of irrigation canal delivery data and processing steps

Constrained by the limited availability of data on water deliveries, we use an extrapolation approach to fill in the data gaps.

1010 The approach integrates two data sources, the irrigation schedules and the actual flow measurements from in-situ data, to produce a complete monthly timeseries. Explicit in this method is the assumption that the canal operations do not vary widely between years in which the conditions are similar. For instance, if years “A”, “B,” and “C” are classified as “dry years,” the canal operations don’t differ much across these years. In other words, if year “A” has unknown estimates, these can be estimated from year “B” or the mean of the three years, depending on the number of years with canal data. Therefore, each 1015 group of distributaries is filled out based on two criteria: the data source and the number of years with available data. For the canals, such as the Deoband parallel, with actual flow measurements and ≥ 5 years of data availability, we solely rely on these data for extrapolation. To this end, we distinguish the years into three conditions (wet, dry, and normal years) using the Palmer Drought Severity Index (PDSI) Terra climate data set as a proxy. Then, every unknown year is filled with the long-term average of the years falling under the same category. For example, when a year such as 2015 is identified as “normal”, this 1020 year is filled with the mean of the canal delivery observed across all other “normal” years. A similar procedure was applied to the EYC lower intakes with actual flows from 2018 to 2022 to fill in missing data for similar years outside this period. For the other intakes with only a few years of data, however, we filled them differently. For instance, the lower intake points of the UGC with flow measurements for only two years, 2021 (dry) and 2022 (wet), we use these years as benchmarks for filling similar wet or dry years. For “normal” years on these intakes, we use the irrigation schedules instead. Explicitly, in cases with 1025 only a single-year irrigation schedule, the flows are obtained by multiplying the full design capacity by the operational time. This step produces conservative and monthly variable flow estimates due to the operational time variation of each distributary. Since the Deoband branch contributes a significant share of the total canal water supplies into the basin, we fill its missing data using the irrigation schedules to avoid the impacts of assuming no variation in operation across the years. In cases where single-year data is available for distributaries such as Bijwara and Baoli, we use the actual flows for this year (2018) as a 1030 reference to fill all other years. As for distributaries without data from design or actual flows, we assume these might not add much to the overall imports into the Hindon basin. At this stage, the canal delivery data is at the daily timestep. The last step is to aggregate to a monthly timescale, sum all intakes, and normalize by the basin area to obtain the gap-filled canal water imports expressed in water depth units (mm month^{-1}).

1035

1040

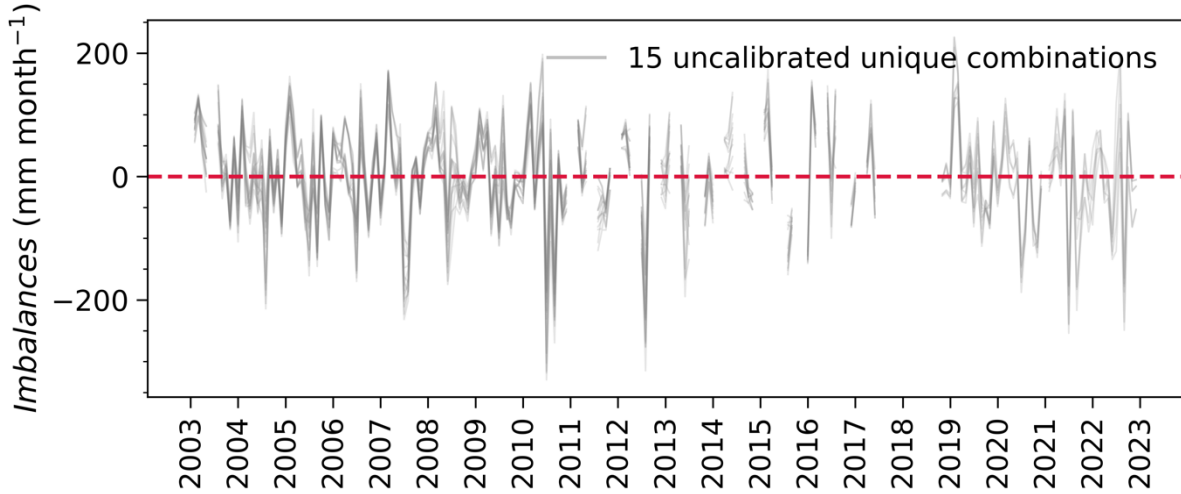
Table A2: Available information on the distributaries and their coverage. The data source column distinguishes between actual (measured) and planned (scheduled) irrigation canal delivery data.

Main Canal	Distributaries	data source	data availability
EYC	Nagla	weekly irrigation schedules	2021-2022
	Babail	weekly irrigation schedules	2021-2022
	Sarkari	weekly irrigation schedules	2021-2022
	Landha	not available	not available
	Meghchhapar	weekly irrigation schedules	2021-2022
	Chhidbana	weekly irrigation schedules	2021-2022
	Nalhera	weekly irrigation schedules	2021-2022
	Reri	weekly irrigation schedules	2021-2022
	Rampuri	weekly irrigation schedules	2021-2022
	Kallarpur	Daily actual flows	2018-2023
	Sijad	not available	not available
	Olra Escape	not available	not available
	Yarpur	Daily actual flows	2018-2023
	Gohari	Daily actual flows	2018-2023
	Malipur	Daily actual flows	2018-2023
	Fazalpur	Daily actual flows	2018-2023
	Bijwara	Daily actual flows	2018
	Baoli	Daily actual flows	2018
UGC	Deoband Branch	Daily actual flows	2013-2014-2016
	Parallel Deoband	Daily actual flows	2018 to 2022 and 2013-2014-2016
	Tanshipur	weekly irrigation schedules	2021-2022
	R. Mohammadpur	weekly irrigation schedules	2021-2022
	R.Jauli	Daily actual flows	2021-2022
	Mansurpur	Daily actual flows	2021-2022
	Khatauli Escape	Daily actual flows	2021-2022
	R. Salawa	Daily actual flows	2021-2022

Appendix B

B1. A major challenge arising from the use of uncalibrated remote sensing water balance data

1045 The following figure shows that imbalance errors due to combining uncalibrated remote sensing products for each water balance variable can be significant ($\sim \pm 200$ (mm month $^{-1}$)). This is related to errors associated with the data. Therefore, there is a need to quantify and reduce these uncertainties.



1050 **Fig B1: Monthly timeseries of the imbalances (water balance errors) for each of the 15 unique uncalibrated combinations of the variables.**

B2. Computing posteriors of individual variables, parameters, and posterior cross-correlations between water balance variables

This section briefly explains how all posteriors are computed. For the probabilistic water balance model described in section 4.1 of the main text, we can represent its joint distribution as $p(x, \theta, S_{obs})$. This distribution consists of two parts: the monthly 1055 water balance variables x (comprising $5N + 1$ variables including $S_0, \bar{P}_t, \bar{E}_t, Q_t, C_t$ and S_t), where N is the number of months and is equal to 240 for 20 years of data considered in this paper, S_0 is the initial basin water storage at the start of the first month and S_{obs} is the storage timeseries, and the parameter vector θ , including $w_p, r_p, w_E, f_E, r_E, a_Q, b_Q, a_C, b_C, \sigma_S, A$, and δ . Our objective is to compute the full posterior distribution, which integrates all available information sources (Gaussian distributions) of θ and x .

1060 The posterior of the parameter vector is expressed in the following form:

$$p(\theta|S_{obs}) \propto p(S_{obs}|\theta)p(\theta) \quad (B1)$$

where $p(\theta)$ is the prior distribution for the parameters and corresponds to the product of the individual parameter priors defined in the previous basin-wide error model section, while the term $p(S_{obs}|\theta)$ refers to the parameter likelihood function. This function scores each set of bias parameters (e.g., w_E, f_E) and noise parameters (e.g., r_E, σ_S). A large likelihood for the

parameters is one that shifts the storage predicted from the water balance closer to the storage observations. As we show below, 1065 this likelihood also connects the DE-MCMC for parameter sampling and EP for posterior computations of water balance variables.

In the basin-wide inference setup, an outer MCMC loop iteratively proposes sets of parameter candidates (samples) using a non-parametric proposal (jumping) mechanism (Ter Braak and Vrugt, 2008). For each set of sampled parameters by MCMC, the EP (message passing) algorithm operates in an inner loop, computing the (a) unnormalized posterior density of the 1070 parameters proposed by MCMC (Eq. (B1)) and the conditional water balance posteriors $p(x | S_{obs}, \theta) = \frac{p(x, S_{obs} | \theta)}{p(S_{obs} | \theta)}$. The normalizing constant of the conditional water balance posterior ($p(S_{obs} | \theta)$) is the likelihood in Eq. (B1). EP evaluates the posterior odds of the model outputs $p(x | S_{obs}, \theta)$ given the sampled parameters, guiding the DE-MCMC decisions in accepting or rejecting new parameters. Compared to the standard single forward-backward algorithm, EP approximates the exact posterior distributions with Gaussian distributions sharing matching moments (mean and variance). It involves multiple 1075 back-and-forward passes over the data using the entire timeseries until all posteriors stabilize. A key aspect of the EP algorithm is its ability to efficiently handle non-Gaussian posteriors, which arise from physical non-negativity constraints we force on water balance variables (\bar{P}, \bar{E}, Q, C). Typically, a small number of iterations are sufficient to achieve convergence due to the mild non-Gaussianity induced by these constraints. The EP algorithm yields conditional water balance posteriors (conditioned on the S_{obs} data and the parameter vector θ). Instead of the conditional posterior distribution, we are interested in the marginal 1080 posterior distribution $p(x | S_{obs})$ over the individual water balance variables (S_0, \bar{P}, \bar{E}, Q , and C). Such distributions are obtained by integrating (~averaging) $p(x | S_{obs}, \theta)$ over the parameter posterior distribution $p(\theta | S_{obs})$, effectively accounting for the parameter uncertainty in the final water balance estimates:

$$p(x | S_{obs}) = \int p(x | S_{obs}, \theta) p(\theta | S_{obs}) d\theta \quad (B2)$$

This paragraph explains how to compute posterior cross-covariances between the different water balance variables given the 1085 posterior marginal distributions of each variable (as output by the water balance data fusion model). For this, we will need two building blocks to construct the joint precision matrix (Θ) equal to the inverse of the covariance matrix (V^*), namely: the variables' linear relation through the water balance coefficients $\varphi = [1, 1, -1, -1, 1]$ extracted from the water balance constraint at each time step: $S = S_0 + \bar{P} - \bar{E} - Q + C$ and "uncorrelated priors" of each variable. The term "priors" reflects uncertainty before considering the relation of each variable with other variables. With the marginal distributions available at 1090 this point, we can back-calculate these priors such that they satisfy the marginals through a message-passing algorithm. This algorithm relies on decomposing the marginal precisions (τ) for each variable into: (a) prior precisions (messages) for each variable and (b) precisions (messages) sent to each variable from all other variables via the water balance. Specifically, in each month, we have two conditions: the water balance constraint and the probabilistic constraints in the form of marginal Gaussian distributions written separately for individual variables x as $p(x) \sim \mathcal{N}(m_x^*, v_x^*)$, with posterior mean and variance obtained

1095 from Eq. (27) in the main text. Expressed in terms of precisions, we can write the decomposed posterior precision of S (τ_S), for example, as: $\tau_S = \tau_{S \rightarrow} + \tau_{\rightarrow S}$ where $\tau_{S \rightarrow}$ is the prior precision from S, and $\tau_{\rightarrow S}$ is the precision to S from the water balance. The latter can be obtained from all other variables by propagating uncertainty through the linear water balance equation. As such, the relationship between the posterior and prior variances of S that fulfill the two defined conditions becomes:

$$\frac{1}{v_S^*} = \frac{1}{v_{S \rightarrow}} + \frac{1}{v_{S_0 \rightarrow} + v_{\bar{P} \rightarrow} + v_{\bar{E} \rightarrow} + v_{Q \rightarrow} + v_{C \rightarrow}} \quad (B3)$$

We can repeat the above step for all other variables to create a linear system of six equations with six unknowns (prior 1100 variances) that we need to solve for:

$$\left\{ \begin{array}{l} \frac{1}{v_S^*} - \frac{1}{v_{S \rightarrow}} - \frac{1}{v_{S_0 \rightarrow} + v_{\bar{P} \rightarrow} + v_{\bar{E} \rightarrow} + v_{Q \rightarrow} + v_{C \rightarrow}} = 0 \\ \frac{1}{v_{S_0}^*} - \frac{1}{v_{S_0 \rightarrow}} - \frac{1}{v_{S \rightarrow} + v_{\bar{P} \rightarrow} + v_{\bar{E} \rightarrow} + v_{Q \rightarrow} + v_{C \rightarrow}} = 0 \\ \frac{1}{v_{\bar{P}}^*} - \frac{1}{v_{\bar{P} \rightarrow}} - \frac{1}{v_{S_0 \rightarrow} + v_{S \rightarrow} + v_{\bar{E} \rightarrow} + v_{Q \rightarrow} + v_{C \rightarrow}} = 0 \\ \frac{1}{v_{\bar{E}}^*} - \frac{1}{v_{\bar{E} \rightarrow}} - \frac{1}{v_{S_0 \rightarrow} + v_{\bar{P} \rightarrow} + v_{S \rightarrow} + v_{Q \rightarrow} + v_{C \rightarrow}} = 0 \\ \frac{1}{v_Q^*} - \frac{1}{v_Q \rightarrow} - \frac{1}{v_{S_0 \rightarrow} + v_{\bar{P} \rightarrow} + v_{\bar{E} \rightarrow} + v_{S \rightarrow} + v_{C \rightarrow}} = 0 \\ \frac{1}{v_C^*} - \frac{1}{v_C \rightarrow} - \frac{1}{v_{S_0 \rightarrow} + v_{\bar{P} \rightarrow} + v_{\bar{E} \rightarrow} + v_{Q \rightarrow} + v_{S \rightarrow}} = 0 \end{array} \right. \quad (B4)$$

Where $v_S^*, v_{S_0}^*, v_{\bar{P}}^*, v_{\bar{E}}^*, v_Q^*, v_C^*$ are the posterior marginal variances of the variables: Storage S, initial storage state for the first month S_0 , \bar{P} , \bar{E} , Q, and C, respectively. While, $v_{S \rightarrow}, v_{S_0 \rightarrow}, v_{\bar{P} \rightarrow}, v_{\bar{E} \rightarrow}, v_{Q \rightarrow}$, and $v_{C \rightarrow}$ are their corresponding prior variances.

The resulting priors are used to generate the joint precision matrix Θ of S0, P, E, Q, and C, which combines two terms:

$$\Theta = \varphi \varphi' \tau_{S \rightarrow} + \text{diag}([\tau_{S_0} \text{ or } \tau_{S_{t-1} \rightarrow}, \tau_{\bar{P} \rightarrow}, \tau_{\bar{E} \rightarrow}, \tau_{Q \rightarrow}, \tau_{C \rightarrow}]) \quad (B7)$$

The first term represents a matrix that encodes how each variable varies with every other variable in the water balance. This 1105 term is scaled by the prior precision from S ($\tau_{S \rightarrow}$), whereas the second term is a diagonal matrix of the other individual water balance variables prior precisions. The inverse of the joint precision matrix gives the posterior covariance matrix between all variables (in a given month), which contains all posterior cross-correlations.

Appendix C

C1. Water balance priors and posteriors

1110 This section displays the results of the seasonal and annual posterior means of the water balance variables compared to their corresponding prior data.

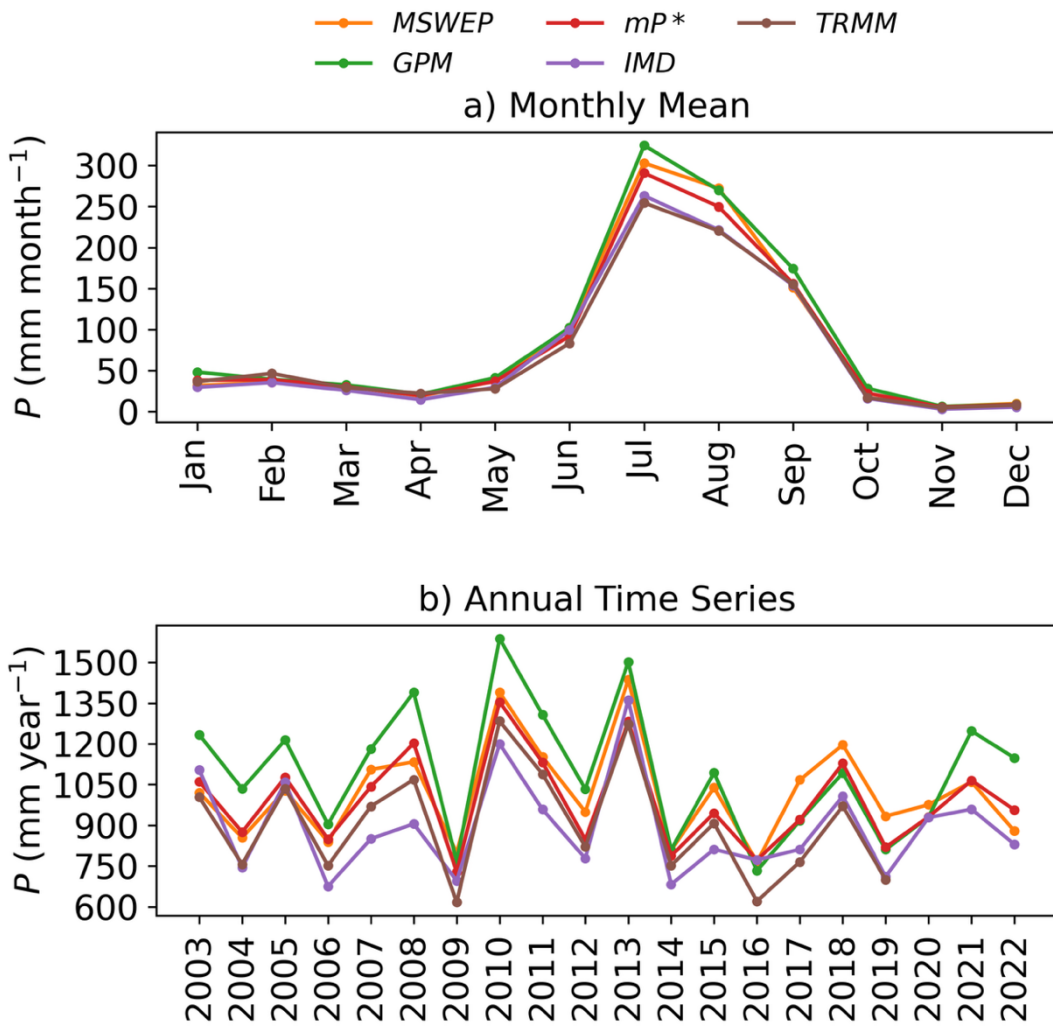
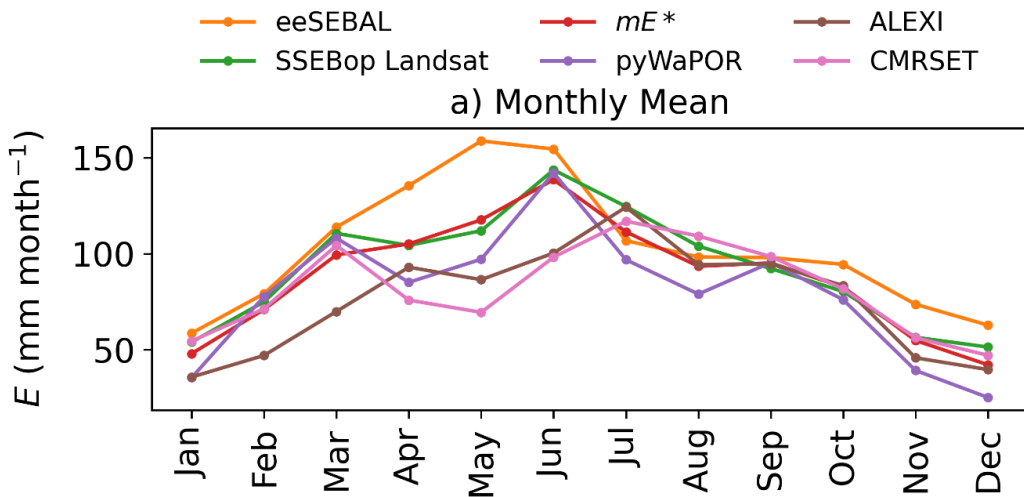


Fig C1: Comparison of posterior mean (mP^*) to the prior data sets describing the precipitation (P) variable in the Hindon basin, the top panel depicts (a) monthly mean P , and the bottom panel (b) shows the annual P time series.



b) Annual Time Series

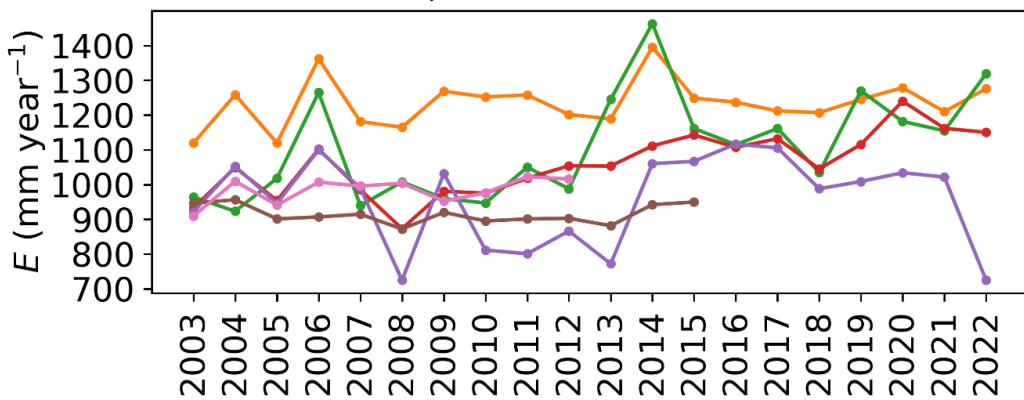


Fig C2: Comparison of the posterior mean (mE^*) to the prior data sets describing the evaporation (E) variable in the Hindon basin, the top panel depicts (a) monthly mean E , and the bottom panel (b) shows the annual E time series.

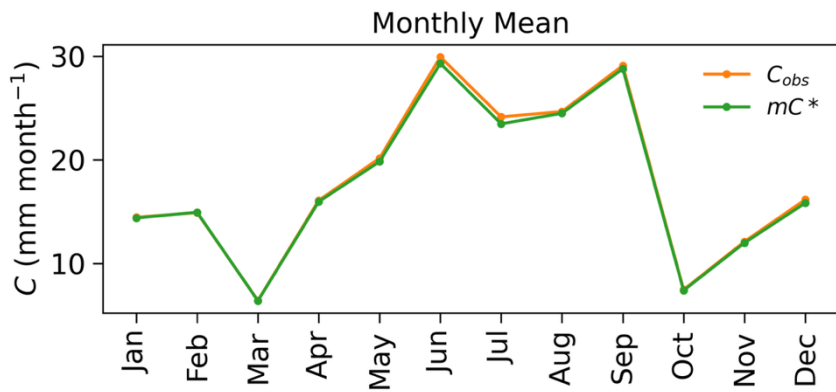


Fig C3: Comparison of the monthly mean posterior mean (mC^*) to the prior data describing the surface water imports (C) variable in the Hindon basin.

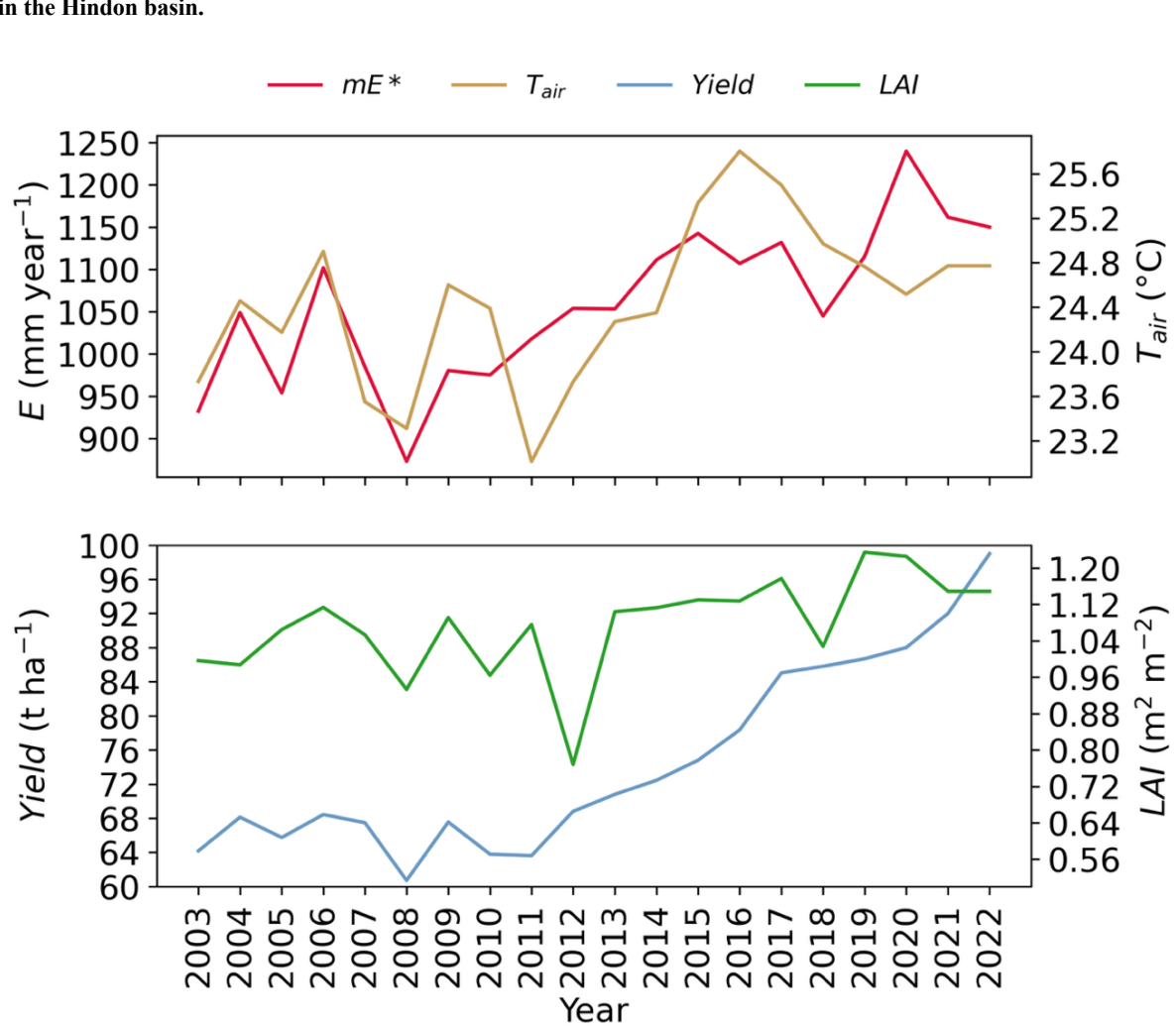
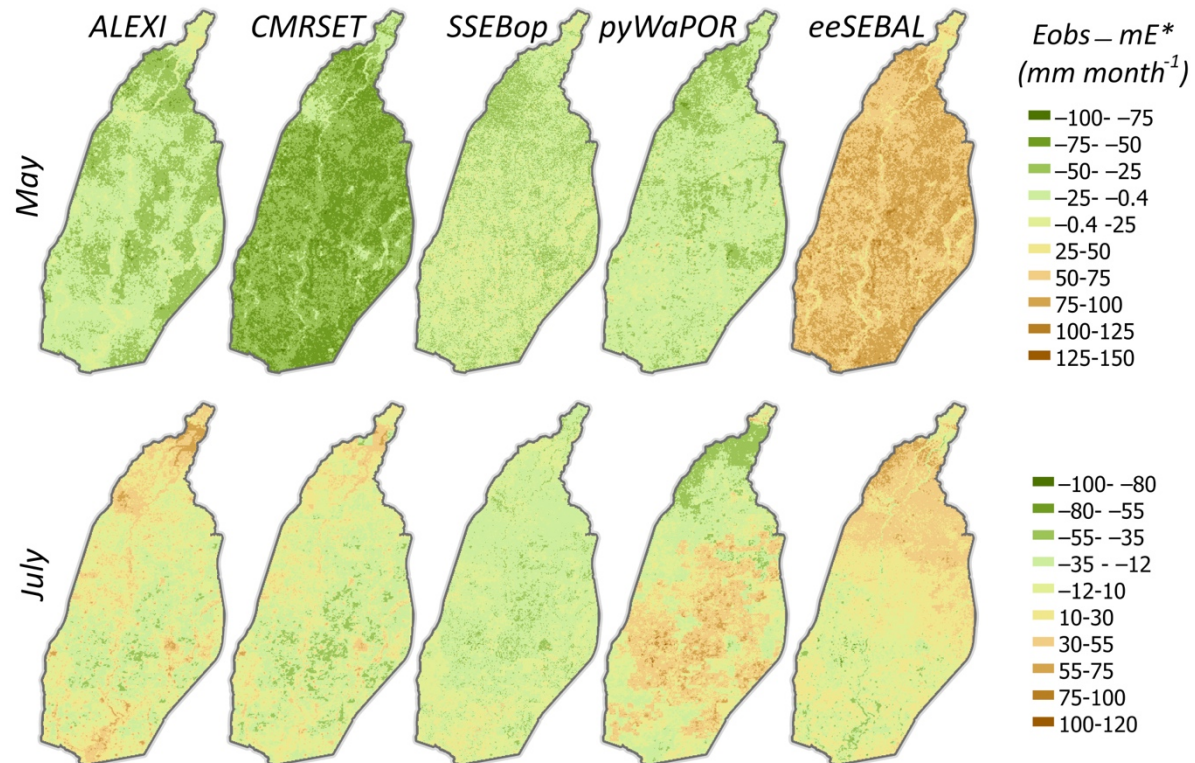


Fig C4: Interplay between the annual: evaporation posterior mean (mE^*), air temperature variable from GLDAS Noah Land Surface Model v2.1 (Rodell et al., 2004), MODIS 15 Leaf Area Index (LAI) (Myneni et al., 2021), and district-wise sugarcane crop yield from International Crops Research Institute for the Semi-Arid Tropics database.

C2. Comparison of individual gridded products to the posterior means

This section presents the spatial maps of the deviation of the individual precipitation and evaporation products from their posterior mean.



1135 **Fig C4: Spatial deviation of the evaporation (E) observations from the posterior mean ($E_{obs} - mE^*$) for May and July of 2009.**

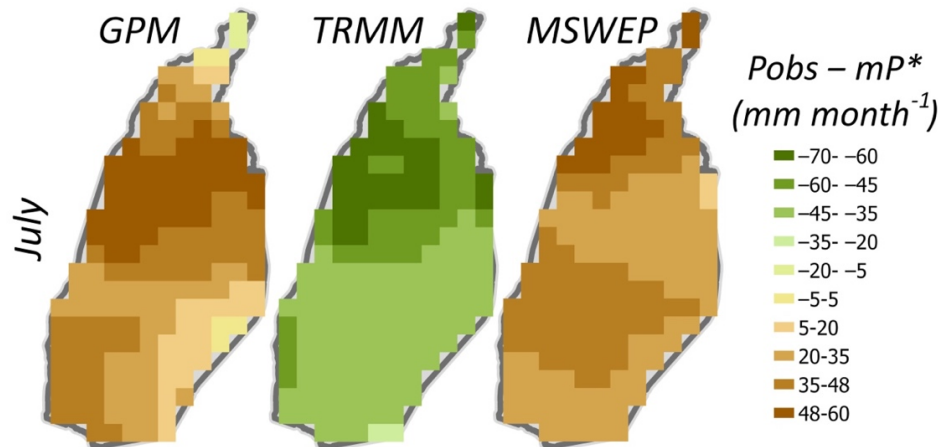
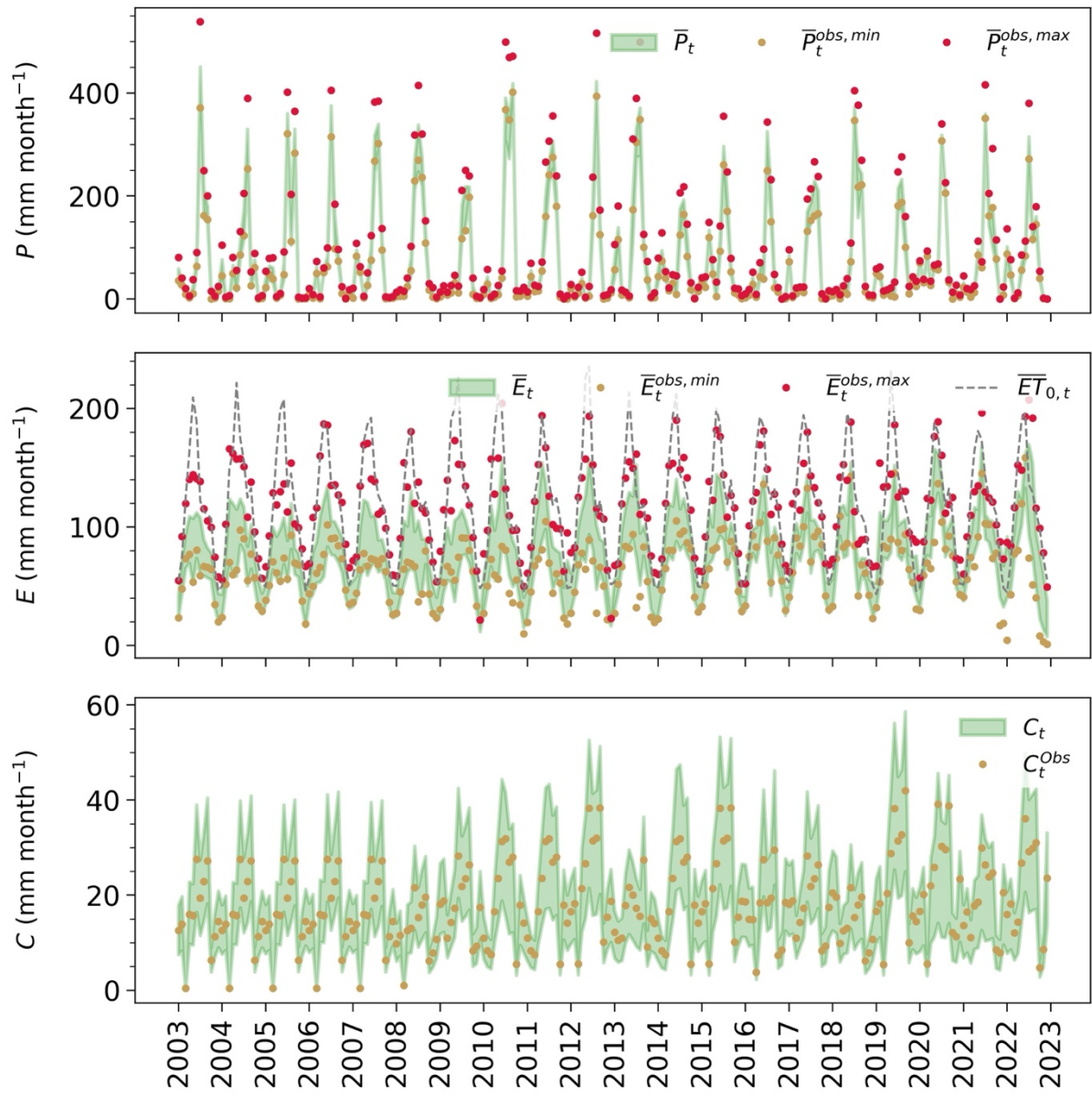


Fig C5: Spatial deviation of the precipitation (P) observations from the posterior mean ($P_{obs} - mP^*$) for May and July of 2009.

C3. The sensitivity of the posterior results to the GRACE input data



1140 Fig C6: Posterior and prior water balance plots correspond to the case using the GRACE CSR spherical harmonic (SH) solution as
an input to the probabilistic water balance model.